bioRxiv preprint doi: https://doi.org/10.1101/2023.12.23.573208; this version posted December 23, 2023. The copyright holder for this preprint (which was not certified by peer review) is the author/funder, who has granted bioRxiv a license to display the preprint in perpetuity. It is made available under aCC-BY-NC-ND 4.0 International license.

Multilayer Network Analysis across Cortical Depths in Resting-State 7T fMRI

Parker Kotlarz[1,2], Kaisu Lankinen[1,3], Maria Hakonen[1,3], Tori Turpin[4], Jonathan R. Polimeni[1,3,5], and Jyrki Ahveninen[1,3]

[1]Athinoula A. Martinos Center for Biomedical Imaging, Massachusetts General Hospital, Charlestown, MA, USA
[2]Harvard Medical School, Boston, MA, USA
[3]Department of Radiology, Harvard Medical School, Boston, MA, USA
[4]McLean Hospital, Boston, MA, USA
[5]Division of Health Sciences and Technology, Massachusetts Institute of Technology, Cambridge, MA, USA

Abstract

In graph theory, "multilayer networks" represent systems involving several interconnected topological levels. A neuroscience example is the hierarchy of connections between different cortical depths or "lamina". This hierarchy is becoming non-invasively accessible in humans using ultra-high-resolution functional MRI (fMRI). Here, we applied multilayer graph theory to examine functional connectivity across different cortical depths in humans, using 7T fMRI (1-mm^3 voxels; 30 participants). Blood oxygenation level dependent (BOLD) signals were derived from five depths between the white matter and pial surface. We then compared networks where the inter-regional connections were limited to a single cortical depth only ("layer-by-layer matrices") to those considering all possible connections between regions and cortical depths ("multilayer matrix"). We utilized global and local graph theory features that quantitatively characterize network attributes such as network composition, nodal centrality, path-based measures, and hub segregation. Detecting functional differences between cortical depths was improved using multilayer connectomics compared to the layer-by-layer versions. Superficial aspects of the cortex dominated information transfer and deeper aspects clustering. These differences were largest in frontotemporal and limbic brain regions. fMRI functional connectivity across different cortical depths may contain neurophysiologically relevant information. Multilayer connectomics could provide a methodological framework for studies on how information flows across this hierarchy.

Keywords (up to 6): fMRI, laminar, connectomics, graph theory, multilayer network

Introduction

Investigating brain activity and functionality through network analyses has become an integral methodological foundation of neuroscience. Connectomics has yielded significant advances in understanding brain structure and function [1, 2]. Modeling the brain as a system of nodes (brain regions) connected by edges (mathematical relationships), often using graph theory, can be used to provide insight into brain characteristics and topological properties [3]. Brain networks can be derived from structural neuroimaging such as MRI or diffusion tensor imaging (DTI) (structural connectomics) [4-6] or functional

bioRxiv preprint doi: https://doi.org/10.1101/2023.12.23.573208; this version posted December 23, 2023. The copyright holder for this preprint (which was not certified by peer review) is the author/funder, who has granted bioRxiv a license to display the preprint in perpetuity. It is made available under aCC-BY-NC-ND 4.0 International license.

neuroimaging such as fMRI, EEG, or magnetoencephalography (MEG) (functional connectomics) [7-11]. Both structural and functional connectomics have been used to understand disease models [12-15], aid in surgical mapping [16-19], and characterize therapeutic effects of neuropsychiatric treatments [20-25].

An emerging field within connectomics, and more broadly graph theory, is the exploration of multilayer networks [26, 27]. Multilayer networks are composed of individual layers of networks with interconnecting edges between different layers. Connections between layers can be solely between homologous nodes (multiplex) or connect nodes regardless of layer or nodal position (multilayer). Multilayer connectomics enables the study of multifaceted and multimodal neuroimaging data, with the different groups of data divided into distinct layers of the connectivity matrix [28-30]. For example, multilayer networks can be derived using correlations between different frequency bands of MEG recordings to identify the interplay between frequencies [31]. Additionally, different modalities such as MEG, fMRI, and diffusion MRI can be combined to identify patterns in brain processing [32] or pathological dysfunction [33] that were not found in traditional single-layer analysis. Thus, multilayer connectomics allows for the incorporation of multidimensional neuroimaging data and can identify relationships between distinct neuroimaging techniques and analyses.

One potential application of multilayer connectomics is understanding the hierarchical organization of the cerebral cortex. Neuroanatomical [34-36] and electrophysiological [37, 38] studies in animal models have identified that laminar input/output patterns can inform about bottom-up (feedforward) or top-down (feedback) processes between cortical regions. Despite its unparalleled resolution, a limitation of laminar electrophysiological recordings in comprehensive connectivity analyses is that the coverage area is typically very small. At the same time, mapping anatomical connections using fiber tracing has limited options for mapping of the post-synaptic targets [39]. Intracortical depth analyses of ultra-high resolution fMRI data have the benefit that the coverage can be extended to the entire cerebral cortex. Advancements in ultra-high-resolution fMRI ($\leq 1\ mm^3$ voxel size) have enabled sampling of functional signals from different depths of the cortical gray matter [40-43]. However, there are multiple challenges and unanswered questions for the feasibility of using cortical depth profiles of fMRI signals [41]. Because deoxygenated blood also drains up to the cortical surface through the intracortical diving venules, voxels intersecting the superficial layers could also be affected by deeper neuronal activations [44]. Despite this limitation, studies using this emerging methodology have attempted to identify feedback and feedforward relationships non-invasively in the human brain [45-56], akin to micro-scale recordings in animal models.

Even with the advent of high-resolution functional neuroimaging, multilayer connectomics have mostly focused on anatomical networks derived from structural MRI and DTI [57, 58] due to their direct relationship to cortical architecture. For example, DTI and histological samples identified that cortical areas with similar laminar structure were more likely to be connected [59]. Additionally, even in functional laminar studies, previous works have predominantly utilized task-based studies in pre-defined brain regions [40, 45-56,

bioRxiv preprint doi: https://doi.org/10.1101/2023.12.23.573208; this version posted December 23, 2023. The copyright holder for this preprint (which was not certified by peer review) is the author/funder, who has granted bioRxiv a license to display the preprint in perpetuity. It is made available under aCC-BY-NC-ND 4.0 International license.

60]. Consequently, the functional components of the whole-brain cortical depths continue to be underexplored.

In contrast to task-based studies, which primarily focus on specific cortical areas [61], resting-state analysis enables whole-brain investigation of laminar organization [43, 62]. These resting-state connections have been shown to reflect anatomical connectivity [63-66]. Thus, network differences within laminar resting-state fMRI networks represent functional differences between cortical depths. This work explores the laminar structure of the cortex using high-resolution resting-state fMRI and multilayer connectomics. We use a dual-pipeline approach in comparing the information extracted from layer-by-layer vs. multilayer connectomics. We demonstrate the validity of multilayer functional laminar connectomics through showing that cortical depths have distinct graph theory characteristics that are more clearly identifiable through multilayer connectomics compared to the traditional single layer methodology.

Methods

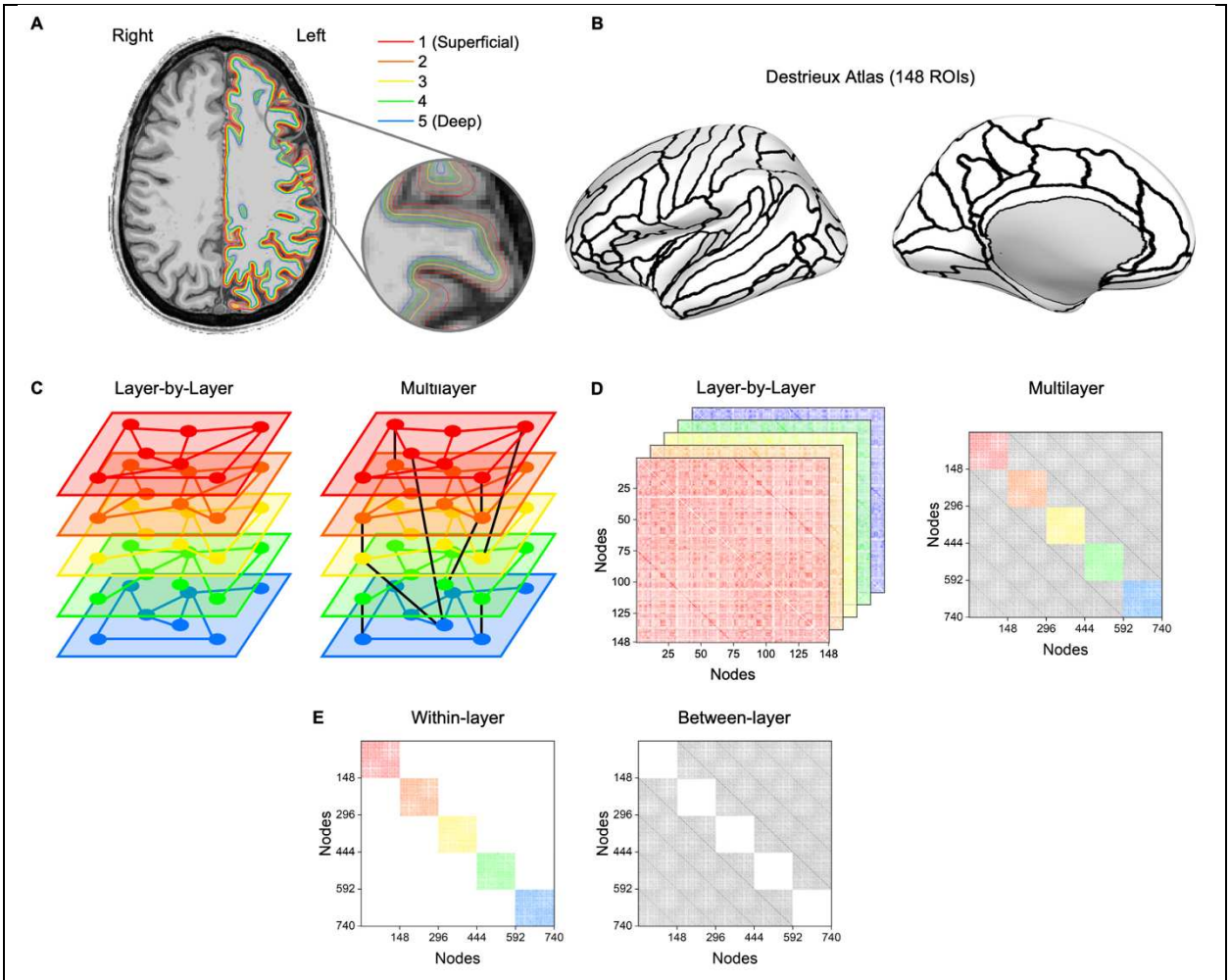

Figure 1. Multilayer connectomic pipeline to analyze functional connectivity across different cortical depths. Here, "layers" refer to the dimensions of the connectivity

bioRxiv preprint doi: https://doi.org/10.1101/2023.12.23.573208; this version posted December 23, 2023. The copyright holder for this preprint (which was not certified by peer review) is the author/funder, who has granted bioRxiv a license to display the preprint in perpetuity. It is made available under aCC-BY-NC-ND 4.0 International license.

matrices which represent fMRI signals gathered from different "cortical depths." **(A)** The cortex was uniformly divided into five surfaces at different depths, as seen above projected on a 0.75-mm isotropic-resolution anatomical T_1-weighted image. **(B)** The brain was parcellated into 148 regions-of-interest (ROIs) (74 per hemisphere) based on the Destrieux atlas in FreeSurfer [67, 68]. The ROIs are shown on an inflated left-hemisphere cortical surface. **(C)** Schematic showing the difference between a layer-by-layer network and a multilayer network. In the layer-by-layer approach, each layer (network) is independent of other layers while in the multilayer approach, the layers are inter-connected. A sparser multilayer network is shown for visualization purposes. **(D)** Example matrix construction from both the layer-by-layer and multilayer approaches. While both approaches use matrices derived from Pearson correlations from the different layers, the multilayer approach generates a supra-adjacency matrix that also has correlations between different layers (shown in grayscale). **(E)** Example matrix construction for within-layer and between-layer matrices. For within-layer matrices, each sub-matrix is extracted individually for analysis. White areas represent connections excluded from the analysis.

Participants

Thirty healthy adults (mean age $\pm$ standard deviation = 32.4 $\pm$ 10 years, 15 women, all right-handed) were recruited using an internal online recruiting platform. Participants were screened for vision problems, hearing problems, cognition-altering medications, and exclusions for MRI (metal in the body). Twenty-eight of the participants were native English-speakers. Informed consent was obtained from all participants, and MRI safety screening forms were completed before each scan. The study design, protocol, and consent were approved by the Mass General Brigham Institutional Review Board.

Image Acquisition

Participants were measured in sets of 7.9-min resting-state fMRI scans occurring on different days (3 to 4 sessions per participant). Twenty-three participants were measured in twelve resting-state scans. Seven participants had between ten to eighteen resting-state scans (10 scans: n = 1; 11 scans: n = 1; 13 scans: n = 2; 14 scans: n = 2, 18 scans: n = 1). The participants were instructed to avoid movement during the scans and keep their eyes open and fixated on a fixation cross projected on a screen viewed through a mirror. The average duration of the sessions was around two hours. Breathing and heart rate were recorded using the built-in Siemens system at a sampling rate of 400 Hz. Inhalation and exhalation were measured with the Siemens respiratory-effort transducer attached to a respiratory belt. The heart rate was recorded using Siemens photoplethysmogram transducers on the participant's index finger.

The functional and structural neuroimaging data was acquired using a 7T whole-body MRI scanner (MAGNETOM Terra, Siemens, Erlangen, Germany) with a home-built custom-built 64-channel array coil [69]. To reduce participant head motion inside the scanner, MRI-compatible paddings were placed around the head and neck. In each

bioRxiv preprint doi: https://doi.org/10.1101/2023.12.23.573208; this version posted December 23, 2023. The copyright holder for this preprint (which was not certified by peer review) is the author/funder, who has granted bioRxiv a license to display the preprint in perpetuity. It is made available under aCC-BY-NC-ND 4.0 International license.

imaging session, T_1-weighted anatomical images were measured using a 0.75-mm isotropic multi-echo MPRAGE pulse sequence [70, 71] with repetition time (TR) = 2530 ms, four echoes with echo time (TE) of 1.72, 3.53, 5.34, and 7.15 ms, 7° flip angle, 240 × 240 mm^2 field of view (FoV), and 224 sagittal slices. To help with pial surface placement by avoiding dura mater, T_2-weighted anatomical images (voxel size = 0.83 x 0.83 x 0.80 mm, TR = 9000 ms, TE = 269 ms, flip angle = 120°, FoV = 225 x 225 mm^2, 270 sagittal slices) were acquired for twenty-eight out of thirty participants in one of the imaging sessions. Resting-state functional imaging was collected using a T_2*-weighted blipped-CAIPI [72] simultaneous multi-slice (SMS) echo planar imaging (EPI) sequence using multi-band RF pulses [72] with 4× acceleration factor in phase-encoding direction, 3× acceleration factor in slice-encoding direction, TR = 2800 ms, TE = 27.0 ms, isotropic 1-mm^3 voxels, 78° flip angle, 192 × 192 mm^2 FoV, 132 axial slices, anterior-to-posterior phase encoding direction, 1446 Hz/pixel bandwidth, 0.82 ms nominal echo spacing, and fat suppression. In addition, to de-warp the functional data, an EPI scan was collected with identical parameters but with an opposite phase-encoding polarity (posterior-to-anterior, PA-EPI) relative to the functional scans. For four participants with missing PA-EPI scans, the data were de-warped using a gradient-echo field map (TR = 1040 ms, TE = 4.71 ms and 5.73 ms, isotropic 1.3-mm^3 voxels; flip angle = 75°, FoV = 240 × 240 mm^2, 120 slices, bandwidth = 303 Hz/pixel).

MRI Preprocessing

First, SPM12 (http://www.fil.ion.ucl.ac.uk/spm/, [SPM12-spm_preproc_run.m]; bias field correction, full-width at half-maximum, FWHM: 18 mm, sampling distance: 2 mm, bias regularization: 1E−4) and customized MATLAB scripts were used to correct the bias field of the structural T_1 and T_2 images. Next, recon-all of FreeSurfer 6.0 [73] with an extension for submillimeter 7 T data [71] was used to automatically create cortical reconstructions for each participant. An average of multiple T_1-weighted anatomical volumes (3 to 4 per participant) alongside a T_2-weighted volume were used in the reconstruction to enhance the quality of the cortical surfaces. Nine intermediate surfaces were created between the white matter and pial surfaces with fixed relative distances, of which five were selected for the laminar analysis (described below). Lastly, the surfaces generated by recon-all were corrected manually for inaccuracies with Recon Edit of Freeview.

For the functional data, slice-timing and motion corrections were first implemented in FreeSurfer 7.1 [73]. De-warping was then used to correct for geometric distortions caused by susceptibility-induced off-resonance fields. In de-warping, the off-resonance distortion field was estimated using the functional data and the PA-EPI scan collected with reversed a phase-encode blip; thus, the distortions are reversed in direction in respect to the scans [FreeSurfer: topup, applytopup] [74, 75]. For four participants that were missing the PA-EPI scan used above, the distortion field was estimated using the B_0 field map scan in FreeSurfer 6.0 [FreeSurfer-epidewarp]. The respiratory and heart rate artifacts were corrected using the RETROspective Image CORrection (RETROICOR) algorithm (3^{rd} order heart rate, respiratory, and multiplicative terms) [76]. Three participants were missing heart rate data and, therefore, only respiratory recordings were used in RETROICOR. In addition, RETROICOR was not applied to five participants with missing

bioRxiv preprint doi: https://doi.org/10.1101/2023.12.23.573208; this version posted December 23, 2023. The copyright holder for this preprint (which was not certified by peer review) is the author/funder, who has granted bioRxiv a license to display the preprint in perpetuity. It is made available under aCC-BY-NC-ND 4.0 International license.

respiratory and heart rate data. Functional data were then co-registered with the structural images using Boundary-Based Registration in FreeSurfer 6.0 [77]. By projecting each intersecting voxel onto the corresponding surface vertex using trilinear interpolation, the fMRI timeseries were then resampled onto the pial and white matter surfaces, and nine cortical depths between them.

From the nine intracortical surfaces, five alternating depths were selected starting closest to pial surface (depths 1 to 5, superficial to deep) (**Figure 1A**). The outside surfaces (pial and white matter) were excluded to avoid partial volume effects from the cerebrospinal fluid and white matter, respectively. Additionally, depths included were alternated to minimize potential for partial volume overlap between surfaces that would bias the correlation matrix generation.

Matrix Generation and Processing

Two parallel matrix processing pipelines were used to generate individual independent adjacency matrices for the layer-by-layer approach while creating one supra-adjacency matrix for the multilayer approach (**Figures 1C and 1D**). The layer-by-layer approach creates an independent network for each cortical depth while the multilayer approach results in five interconnected networks that combines all cortical depths.

One important distinction is between the terminology “depth” and “layer.” Here, depth refers to the anatomical depth in the cortex while layer refers to a specific network derived from a cortical depth. This distinction is critical to avoid equating a network layer with an associated cerebral cortical layer.

The brain was parcellated into 148 regions-of-interest (ROIs) (74 per hemisphere) based on the Destrieux atlas in FreeSurfer [67, 68] (**Figure 1B**). A detailed list of parcellations can be found in the **Table S1**.

Resting-state time series for each participant were concatenated across runs, leading to the following number of time points: 2028 for n = 23 participants; 1690 time points: n = 1; 1859 time points: n = 1; 2197 time points: n = 2; 2366 time points: n = 2, and 3042 time points: n = 1. Concatenated time series were detrended and filtered using a second-order Butterworth filter [high-pass: 0.01 Hz, low-pass: 0.1 Hz, MATLAB-filtfilt].

For the **layer-by-layer approach**, Pearson correlations were derived between ROIs within the same depth, resulting in 10878 pairwise correlations from 148 nodes (ROIs) after removing 148 self-correlations (number of correlations = (nodes^2 – diagonal nodes) / 2). Pearson correlation coefficients were normalized using Fisher’s z-transformation resulting in five 148-by-148 symmetric weighted connectivity matrices for each participant, i.e., one matrix for each cortical depth (**Figure 1D**).

For the **multilayer approach**, Pearson correlations were derived between ROIs between and within all depths, resulting in 273430 pairwise correlations from 740 nodes (140 ROIs times 5 depths) after removing 740 self-correlations. Pearson correlation coefficients

bioRxiv preprint doi: https://doi.org/10.1101/2023.12.23.573208; this version posted December 23, 2023. The copyright holder for this preprint (which was not certified by peer review) is the author/funder, who has granted bioRxiv a license to display the preprint in perpetuity. It is made available under aCC-BY-NC-ND 4.0 International license.

were then normalized using Fisher's z-transformation with the final product being a 740 by 740 symmetric weighted connectivity matrix for each participant (**Figure 1D**).

For both approaches, individual matrices were normalized and thresholded at 2% intervals ranging from 2 to 40% graph density (ratio of edges present to total number of possible edges) to understand measure differences over a wide range of thresholds. Thresholding is required to minimize the effect spurious correlations.

We also examined the account of within- and between-layer connections only in the context of the complete multilayer matrix. To this end, we draw two additional types of sub-matrices from the multi-layer matrix, selectively concentrating on either their within-layer aspect (here, termed **multilayer within-layer**) or the between-layer aspects (termed **multilayer between-layer**) only. The **multilayer within-layer** matrices were derived by normalizing the supra-adjacency matrix, thresholding the matrix, and then extracting the nodes included in each individual layer (i.e. nodes 1 to 148 for layer 1), creating a 148-by-148 weighted connectivity matrix. The **multilayer between-layer** matrices were, in turn, derived by normalizing the supra-adjacency matrix, thresholding the matrix, and then zeroing the five diagonal matrices (from each cortical depth) composing within-layer connections, thus resulting in only between-layer connections. (It is worth noting that since the within-layer and between-layer connectivity matrices were extracted after thresholding, analysis that requires normalization, i.e., non-thresholded matrices, could be conducted in the context of this analysis; **Figure 1E**.)

Edge Consistency and Variability

Connections (edges) within and between layers were explored to understand edge consistency and variability between participants. Edge consistency [78] was calculated by selecting the top five percent of edges with the lowest standard deviation in un-thresholded multilayer networks. In contrast, edge variability [79] was calculated by selected the top five percent of edges with the highest standard deviation across participants. In both cases, edges in each layer were then summed and divided by the total number of significant edges to identify the percentage of significant edges in each layer.

Matrix Similarity

Matrix similarity was used to understand how matrices differed across layers. Thresholded (2–40%) and normalized matrices were compared using cosine similarity,

$$CS_{i,j} = \frac{X_i \cdot X_j}{||X_i||\,||X_j||}$$

where X_i and X_j are vectors of the upper triangular elements of two adjacency matrices [MATLAB-pdist2], with values ranging from −1 (maximal dissimilarity) to +1 (maximal similarity). Cosine similarity was shown to distinguish between matrices better than traditionally used Pearson correlation [79, 80]. Using both the layer-by-layer approach

bioRxiv preprint doi: https://doi.org/10.1101/2023.12.23.573208; this version posted December 23, 2023. The copyright holder for this preprint (which was not certified by peer review) is the author/funder, who has granted bioRxiv a license to display the preprint in perpetuity. It is made available under aCC-BY-NC-ND 4.0 International license.

and within-layer matrices, each layer was compared to the other layers. Additionally, to understand how matrix generation differs between methods, the same layer was compared across layer-by-layer and within-layer approaches.

Connectomic Analysis

Global and nodal measures were calculated in MATLAB using the Brain Connectivity Toolbox (MATLAB Version R2022b) [3] on the Massachusetts Life Sciences Center Compute Cluster (DELL R440 servers with two Intel Xeon Silver 4214R twelve core CPUs). Global measures characterize the entire network while nodal measures characterize attributes of specific node (ROI). Nodal measures can also be averaged to create a global measure. Measures can be grouped into four general categories to describe their overall network characterization: composition, centrality, integration, and segregation. **Composition** measures describe the topology of the network while **centrality** measures detail specific nodal importance for network function. **Integration** measures examine how information flows through the network and **segregation** measures explore how the network is divided into functional components. Therefore, different measures can be used to understand different characteristics of the network. For example, decreased nodal and global average strength was found in maltreated children indicating decreased overall brain connectivity [81] while decreased clustering coefficient and global efficiency in patients with Parkinson's disease can signify deficits in brain network integration and segregation [82]. **Table 1** denotes the measures used in this work, and detailed explanation of each measure can be found in Rubinov and Sporns [3].

Table 1. List of network measures used in this work organized by functional category. (n) denotes a nodal measures.

Composition	Centrality	Integration	Segregation
- Largest Cluster Size - Graph Density - Degree (n) - Strength (n)	- Betweenness Centrality (n) - Eigenvector Centrality (n) - Participation Coefficient (n)	- Characteristic Path Length - Radius - Diameter - Global Efficiency - Assortativity	- Maximized Modularity Q - Transitivity - Clustering Coefficient (n) - Local Efficiency (n)

Statistical Analysis

To avoid the bias of selecting a single threshold, area-under-the-curve (AUC) analysis was conducted to create a threshold-independent measure. The measures in **Table 1** were calculated at each threshold (from 2 to 40% graph density in 2% intervals). The measure values at each threshold were then plotted against their threshold, and the area underneath the generated curve was calculated using a trapezoidal integration method [MATLAB-trapz].

For each global measure (and averaged nodal measure), the AUC value for each layer for all participants was compared using a one-way analysis of variance (ANOVA)

bioRxiv preprint doi: https://doi.org/10.1101/2023.12.23.573208; this version posted December 23, 2023. The copyright holder for this preprint (which was not certified by peer review) is the author/funder, who has granted bioRxiv a license to display the preprint in perpetuity. It is made available under aCC-BY-NC-ND 4.0 International license.

[MATLAB-anova1]. A one-way ANOVA was also used to compare each nodal measure to find differences at each specific ROI (node). For the multilayer network and between-layer measures, only nodal values (both averaged and individual) were compared since global measures for the multilayer network (and thus between-layer measures) contain effects from every layer. For nodal values (non-averaged), a False Discovery Rate (FDR, Bonferroni-Holm method) correction (alpha = 0.01) was applied to account for multiple comparisons [83, 84].

Cortical Thickness Validation

One potential confounding factor using whole-brain laminar analysis is that different brain regions have different cortical thicknesses [85-87]. Thus, comparing cortical thickness values of significant brain regions (defined above) can help evaluate whether our findings may be influenced by cortical thickness. Subsequently, cortical thickness values for each ROI for each participant were extracted using FreeSurfer and averaged across all subjects [73]. The distribution of significant nodes versus non-significant nodes for each nodal measure and pipeline with greater than ten significant nodes were compared using a t-test [MATLAB-ttest2].

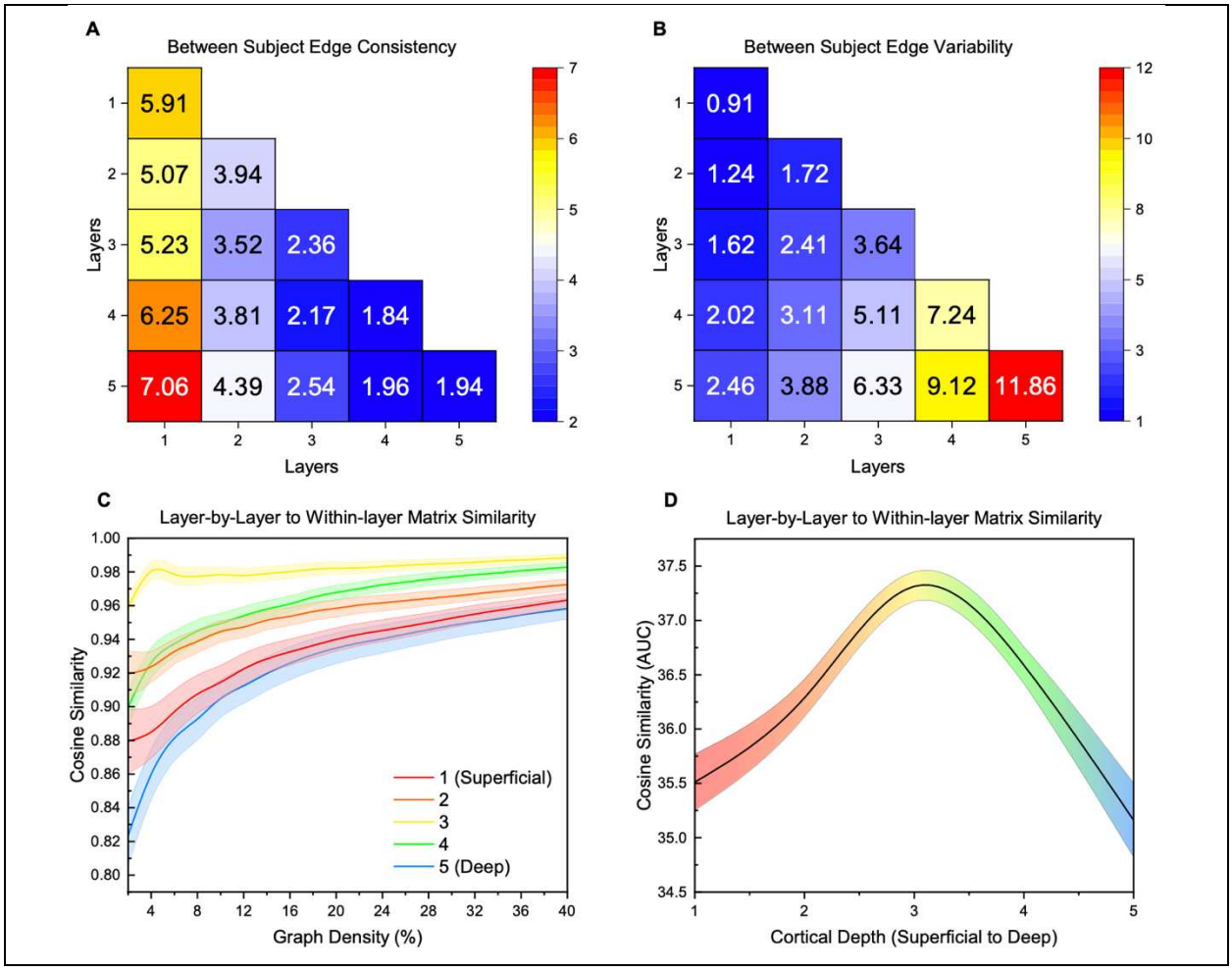

bioRxiv preprint doi: https://doi.org/10.1101/2023.12.23.573208; this version posted December 23, 2023. The copyright holder for this preprint (which was not certified by peer review) is the author/funder, who has granted bioRxiv a license to display the preprint in perpetuity. It is made available under aCC-BY-NC-ND 4.0 International license.

Figure 2. (A) Edge consistency between each participant (multilayer matrix). The edges of each layer of the multilayer matrix were compared to find the edge strengths that had the lowest 5% standard deviation between participants. Higher values indicate a higher percentage of consistent edges, indicating consistent features between participants for those connections. **(B)** Edge variability between each participant (multilayer matrix). The edges of each layer of the multilayer matrix were compared to find the edge strengths that had the highest 5% standard deviation between participants. Higher values indicate a higher percentage of variable edges, indicating variable features between participants for those connections. **(C)** Cosine similarity between layer-by-layer and within-layer matrices (multilayer approach). Within participant, the matrix generation methods were compared using cosine similarity across a range of thresholds at each layer. Cosine similarity values range from −1 (maximal dissimilarity) to +1 (maximal similarity). The mean value at each threshold is plotted while the shaded region indicates the standard error. **(D)** Area-under-the-curve (AUC) measure in comparing layer-by-layer and within-layer matrix generation methods. Spline interpolation was used for visualization. The AUC from **(C)** is calculated using trapezoidal approximation. Higher values indicate higher similarity between methods while lower values indicate lower similarity between methods. The mean AUC value at each layer is plotted while the shaded region indicates the standard error.

Results

Matrix Similarity and Edge Comparison

Edges from the multilayer matrix were compared to understand differences and similarities between participants and to see if the laminar connectomic methodology can distinguish different participants. High edge consistency indicates a similar connectivity pattern between participants while a high edge variability increases the ability to distinguish been participants. **Figure 2A** and **Table 2** shows the percentage of consistent edge strengths between participants that each layer contains from the multilayer matrix. Layer 1 (derived from the depth closest to pial surface) has the largest number of consistent edges (29.52%) with connections between layer 1 and layer 5 (7.06%) being the most consistent between participants. In contrast, **Figure 2B** shows the edge variability between participants with the highest variability found in layer 5 (closest to white matter) overall (33.65%) and in within layer connections (11.86%). It is important to clarify that edge consistency and variability are not mutually related, even though they provide complementary results above.

After edge analysis, connectivity matrices were compared within participants to understand the two competing matrix generation methodologies: layer-by-layer vs. within-layer (multilayer) approach. Cosine similarity was used to examine similarities between different connectivity matrices. In comparing within participant matrices across layers (**Figure S1**), layers were found to be similar with the most distant layers (layer 1 to layer 5) having the lowest similarity in both layer-by-layer matrices and within-layer matrices. Matrices within the same layer and within participant were also compared across the

bioRxiv preprint doi: https://doi.org/10.1101/2023.12.23.573208; this version posted December 23, 2023. The copyright holder for this preprint (which was not certified by peer review) is the author/funder, who has granted bioRxiv a license to display the preprint in perpetuity. It is made available under aCC-BY-NC-ND 4.0 International license.

matrix generation methods (**Figure 2C** and **2D**). Layer 3 was the most consistent across the two methodologies while the peripheral layers (layer 1 and layer 5) differed the most between methods.

Table 2. Edge consistency and variability percentages for each layer derived from the multilayer matrix. Bolded values show the highest percentage for each measure.

Layer	Edge Consistency (%)	Edge Variability (%)
1 (Superficial)	**29.52**	8.25
2	20.73	12.36
3	15.82	19.11
4	16.03	26.60
5 (Deep)	17.89	**33.65**

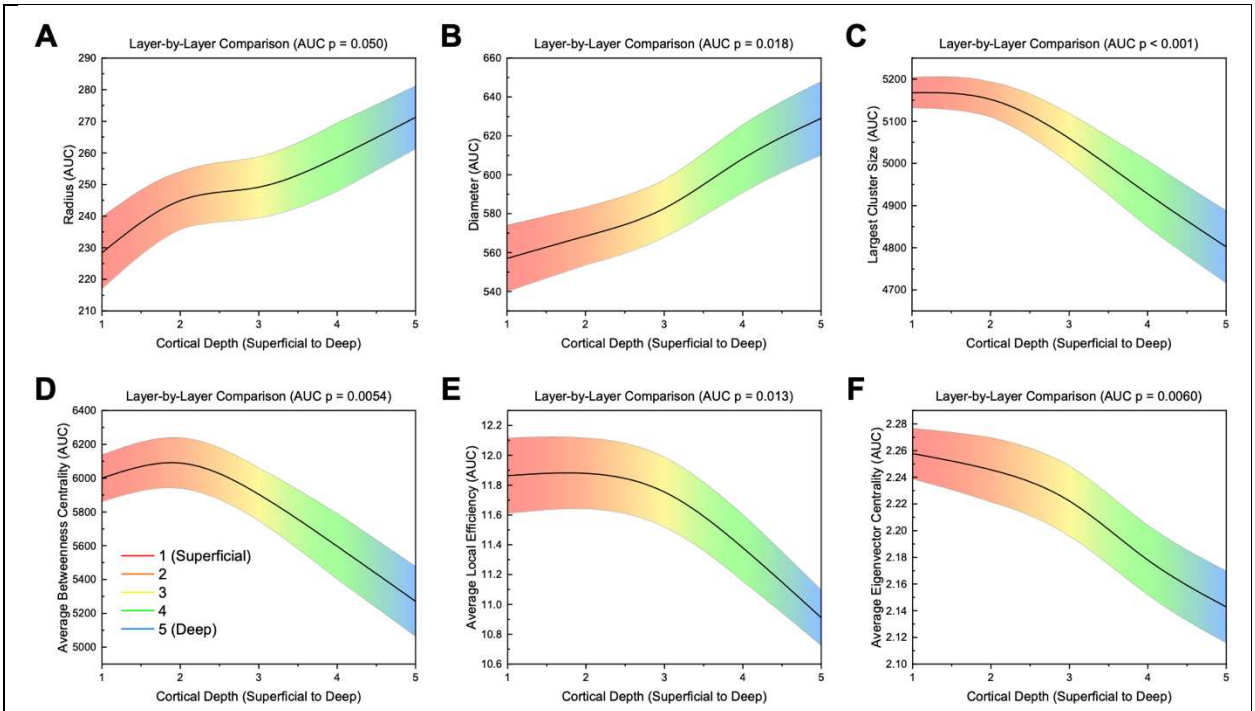

Figure 3. Area-under-the-curve (AUC) values across different layers for significant global measures ($p \leq 0.05$) for layer-by-layer analysis. Significance was calculated using a one-way ANOVA. Spline interpolation was used for visualization. The mean value across participants at each layer is plotted while the shaded region indicates the standard error.

Single Layer Results

Global

Global network measures were calculated for layer-by-layer matrices. AUC values for each global measure can be found summarized in **Table S2**. Network radius (p = 0.050) and diameter (p = 0.018) significantly increased from the most superficial layer 1 to the

bioRxiv preprint doi: https://doi.org/10.1101/2023.12.23.573208; this version posted December 23, 2023. The copyright holder for this preprint (which was not certified by peer review) is the author/funder, who has granted bioRxiv a license to display the preprint in perpetuity. It is made available under aCC-BY-NC-ND 4.0 International license.

deepest layer 5 (**Figure 3A–B**). Largest cluster size ($p < 0.001$), average betweenness centrality ($p = 0.0054$), average local efficiency ($p = 0.013$), and eigenvector centrality ($p = 0.0060$) significantly decreased from layer 1 to layer 5 (**Figure 3C–F**), with a peak in layer 2 for average betweenness centrality and average local efficiency. There were no significant differences in modularity, transitivity, characteristic path length, assortativity, average degree centrality, average strength, average clustering coefficient, and average participation coefficient (**Figure S2–3).** Graph density and average degree centrality were constant across layers due to both measures being a direct function of thresholding (**Figure S2–3**).

Nodal

Table 3 shows the number of nodes in brain regions in layer-by-layer matrices with significant differences between layers (FDR correction with alpha = 0.01) (See **Table S3** for specific values and regions). Degree centrality, strength, and eigenvector centrality had the greatest number of significant nodes (4/148) (**Table 3**). The limbic region had more significant nodes than all other regions for each measure, except for clustering coefficient which was tied with the temporal region (one significant node for each region). In all measures, the right hemisphere had more significant nodes than the left hemisphere (**Table 3**). In general, the most superficial layers (1 and 2) had the highest value for significant nodes (**Table 3, TableS3, Figure S4–S5**). Significant nodes were distributed across node thickness levels (**Figure S6–S7**).

Table 3. Number of significant nodes within each brain region for layer-by-layer analysis. Significance was calculated from the area-under-the curve (AUC) values using a one-way ANOVA with an FDR correction (alpha = 0.01) to account for multiple comparisons [83, 84]. Details of nodal mapping to each region can be found in Table S1. Orange: hemisphere with the highest number of nodes; Yellow: measure with the highest number of nodes; Green: region within each measure with the highest number of nodes.

Network Measure	Hemisphere	All Regions	Frontal	Limbic	Occipital	Parietal	Temporal
Degree Centrality	Left:	1/74	0/24	1/14	0/10	0/10	0/16
	Right:	3/74	0/24	2/14	0/10	0/10	1/16
	Both:	4/148	0/48	3/28	0/20	0/20	1/32
Strength	Left:	1/74	0/24	1/14	0/10	0/10	0/16
	Right:	3/74	0/24	2/14	0/10	0/10	1/16
	Both:	4/148	0/48	3/28	0/20	0/20	1/32
Eigenvector Centrality	Left:	1/74	0/24	1/14	0/10	0/10	0/16
	Right:	3/74	0/24	2/14	0/10	0/10	1/16
	Both:	4/148	0/48	3/28	0/20	0/20	1/32
Betweenness Centrality	Left:	0/74	0/24	0/14	0/10	0/10	0/16
	Right:	3/74	1/24	2/14	0/10	0/10	0/16
	Both:	3/148	1/48	2/28	0/20	0/20	0/32
Clustering Coefficient	Left:	0/74	0/24	0/14	0/10	0/10	0/16
	Right:	2/74	0/24	1/14	0/10	0/10	1/16
	Both:	2/148	0/48	1/28	0/20	0/20	1/32
Local Efficiency	Left:	1/74	0/24	1/14	0/10	0/10	0/16
	Right:	3/74	0/24	2/14	0/10	0/10	1/16

bioRxiv preprint doi: https://doi.org/10.1101/2023.12.23.573208; this version posted December 23, 2023. The copyright holder for this preprint (which was not certified by peer review) is the author/funder, who has granted bioRxiv a license to display the preprint in perpetuity. It is made available under aCC-BY-NC-ND 4.0 International license.

	Both:	4/148	0/48	3/28	0/20	0/20	1/32
Participation Coefficient	Left:	1/74	0/24	1/14	0/10	0/10	0/16
	Right:	2/74	0/24	2/14	0/10	0/10	0/16
	Both:	3/148	0/48	3/28	0/20	0/20	0/32

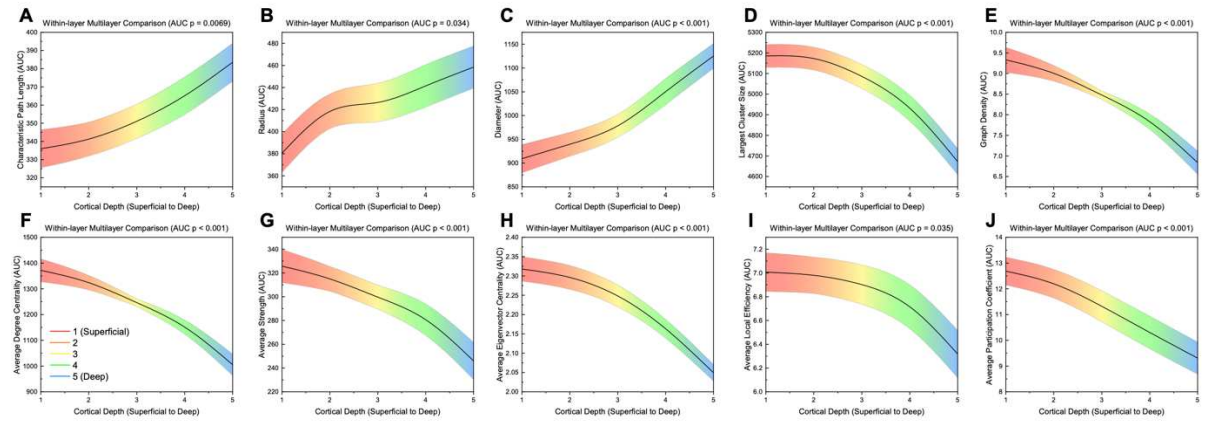

Figure 4. Area-under-the-curve (AUC) values across different layers for significant global measures ($p \leq 0.05$) for within-layer analysis. Significance was calculated using a one-way ANOVA. Spline interpolation was used for visualization. The mean value across participants at each layer is plotted while the shaded region indicates the standard error.

Multilayer Results

Within-layer Global

Figure 4 shows global network measures calculated for within-layer matrices. AUC values for each global measure can be found summarized in **Table S4**. Characteristic path length ($p = 0.0069$), radius ($p = 0.034$), and diameter ($p < 0.001$) all increased from layer 1 to layer 5 (**Figure 4A–C**). Largest cluster size ($p < 0.001$), graph density ($p < 0.001$), average degree centrality ($p < 0.001$), average strength ($p < 0.001$), average eigenvector centrality ($p < 0.001$), average local efficiency ($p = 0.035$), and average participation coefficient ($p < 0.001$) significantly decreased with cortical depth (layer 1 to 5) (**Figure 4D–J**). There were no significant differences for modularity, transitivity, global efficiency, assortativity, average betweenness centrality, and average clustering coefficient (**Figure S8–9**). In contrast to layer-by-layer results, graph density and average degree centrality were different across layers due to the within-layer matrix generation methodology allowing each individual layer to have a different graph density.

Within-layer Local

The number of nodes in brain regions with significant differences using within-layer matrices can be found in **Table 4** (FDR correction with alpha = 0.01, see **Table S5** for

bioRxiv preprint doi: https://doi.org/10.1101/2023.12.23.573208; this version posted December 23, 2023. The copyright holder for this preprint (which was not certified by peer review) is the author/funder, who has granted bioRxiv a license to display the preprint in perpetuity. It is made available under aCC-BY-NC-ND 4.0 International license.

specific values and regions). Degree centrality had the largest number of significant nodes (15/148) followed by strength (9/148), participation coefficient (9/148), and local efficiency (8/148) (**Table 4**). In all measures except participation coefficient, the limbic region had the most significant nodes; in participation coefficient, the temporal region had the most significant nodes (4/32). In all measures, the right hemisphere had more significant nodes than the left hemisphere (**Table 4**). For significant nodes, either layers 1 or 2 had the highest value (**Table 4**, **Table S5, Figure S10–11).** Significant nodes were spread across different node thicknesses (**Figure S12–S13**).

Table 4. Number of significant nodes within each brain region for within-layer analysis. Significance was calculated from the area-under-the curve (AUC) values using a one-way ANOVA with an FDR correction (alpha = 0.01) to account for multiple comparisons [83, 84]. Details of nodal mapping to each region can be found in Table S1. Orange: hemisphere with the highest number of nodes; Yellow: measure with the highest number of nodes; Green: region within each measure with the highest number of nodes.

Network Measure	Hemisphere	All Regions	Frontal	Limbic	Occipital	Parietal	Temporal
Degree Centrality	Left:	4/74	0/24	4/14	0/10	0/10	0/16
	Right:	11/74	1/24	5/14	0/10	0/10	5/16
	Both:	15/148	1/48	9/28	0/20	0/20	5/32
Strength	Left:	2/74	0/24	2/14	0/10	0/10	0/16
	Right:	7/74	0/24	3/14	0/10	0/10	4/16
	Both:	9/148	0/48	5/28	0/20	0/20	4/32
Eigenvector Centrality	Left:	1/74	0/24	1/14	0/10	0/10	0/16
	Right:	3/74	0/24	2/14	0/10	0/10	1/16
	Both:	4/148	0/48	3/28	0/20	0/20	1/32
Betweenness Centrality	Left:	0/74	0/24	0/14	0/10	0/10	0/16
	Right:	3/74	1/24	2/14	0/10	0/10	0/16
	Both:	3/148	1/48	2/28	0/20	0/20	0/32
Clustering Coefficient	Left:	1/74	0/24	1/14	0/10	0/10	0/16
	Right:	5/74	0/24	3/14	0/10	0/10	2/16
	Both:	6/148	0/48	4/28	0/20	0/20	2/32
Local Efficiency	Left:	1/74	0/24	1/14	0/10	0/10	0/16
	Right:	7/74	0/24	4/14	0/10	0/10	3/16
	Both:	8/148	0/48	5/28	0/20	0/20	3/32
Participation Coefficient	Left:	2/74	0/24	1/14	0/10	0/10	1/16
	Right:	7/74	1/24	2/14	1/10	0/10	3/16
	Both:	9/148	1/48	3/28	1/20	0/20	4/32

bioRxiv preprint doi: https://doi.org/10.1101/2023.12.23.573208; this version posted December 23, 2023. The copyright holder for this preprint (which was not certified by peer review) is the author/funder, who has granted bioRxiv a license to display the preprint in perpetuity. It is made available under aCC-BY-NC-ND 4.0 International license.

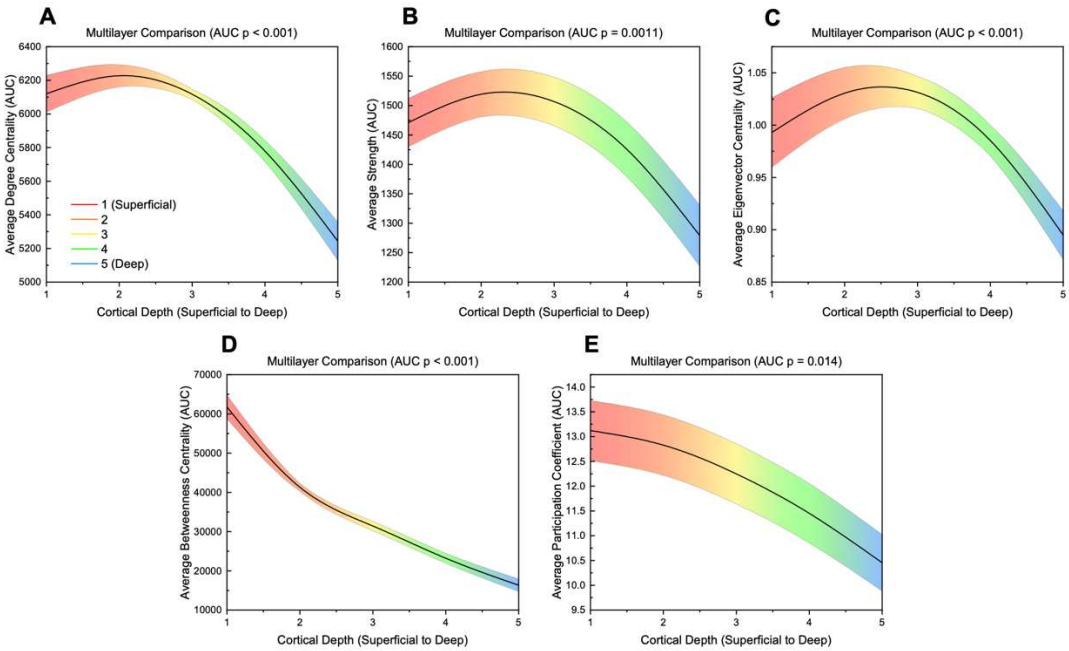

Figure 5. Area-under-the-curve (AUC) values across different layers for significant global measures ($p \leq 0.05$) for multilayer analysis. Significance was calculated using a one-way ANOVA. Spline interpolation was used for visualization. The mean value across participants at each layer is plotted while the shaded region indicates the standard error.

Multilayer Global

Alongside measures for individual layers, global measures were calculated for the supra-adjacency matrix created using the multilayer approach. While only global values derived from nodal averages were statistically compared between layers, AUC values for all global measures are summarized in **Table S6**. Average degree centrality ($p < 0.001$), average strength ($p = 0.0011$), and average eigenvector centrality ($p < 0.001$) decreased from layer 1 to layer 5 with a slight peak at layer 2 (**Figure 5A–C**). Average betweenness centrality ($p < 0.001$) and average participation coefficient ($p = 0.014$) also decreased from layer 1 to layer 5 (**Figure 5D–E**). In contrast, average clustering coefficient tended to increase from layer 1 to layer 5 ($p = 0.069$) (**Figure S14–15, Table S6**). Average local efficiency showed no significant difference between layers (**Figure S14–15, Table S6**).

Multilayer Local

Table 5 depicts the number of nodes in specific brain regions that were significantly different between layers for the multilayer analysis (FDR correction with alpha = 0.01) (See **Table S7** for specific values and regions). Betweenness centrality identified the most significant nodes (58/148) with 19/48 frontal nodes, 16/28 limbic nodes, 2/20 occipital nodes, 5/20 parietal nodes, and 16/32 temporal nodes (**Table 5**). The limbic region had highest percentage of nodes in all measures except clustering coefficient (4/32 in

bioRxiv preprint doi: https://doi.org/10.1101/2023.12.23.573208; this version posted December 23, 2023. The copyright holder for this preprint (which was not certified by peer review) is the author/funder, who has granted bioRxiv a license to display the preprint in perpetuity. It is made available under aCC-BY-NC-ND 4.0 International license.

temporal) and local efficiency (no significant nodes found). Additionally, using betweenness centrality the frontal region had the highest number of significant nodes (19/48). Again, in all measures, the right hemisphere had more nodes with significant differences between layers (**Table 5**). While most significant regions across measures were highest in the superficial layers (layers 1,2), especially in betweenness centrality, the deepest layer (layer 5) had the highest values for nodes significant in clustering coefficient (**Table 5, Table S7, Figure S16**). The thickness of significant nodes was spread across the spectrum of thickness levels, with a preference towards thicker nodes for betweenness centrality (**Figure S17–S18**).

Table 5. Number of significant nodes within each brain region for multilayer analysis. Significance was calculated from the area-under-the curve (AUC) values using a one-way ANOVA with an FDR correction (alpha = 0.01) to account for multiple comparisons [83, 84]. Details of nodal mapping to each region can be found in Table S1. Orange: hemisphere with the highest number of nodes; Yellow: measure with the highest number of nodes; Green: region within each measure with the highest number of nodes.

Network Measure	Hemisphere	All Regions	Frontal	Limbic	Occipital	Parietal	Temporal
Degree Centrality	Left:	2/74	0/24	2/14	0/10	0/10	0/16
	Right:	4/74	0/24	2/14	0/10	0/10	2/16
	Both:	6/148	0/48	4/28	0/20	0/20	2/32
Strength	Left:	1/74	0/24	1/14	0/10	0/10	0/16
	Right:	4/74	0/24	2/14	0/10	0/10	2/16
	Both:	5/148	0/48	3/28	0/20	0/20	2/32
Eigenvector Centrality	Left:	1/74	0/24	1/14	0/10	0/10	0/16
	Right:	2/74	0/24	2/14	0/10	0/10	0/16
	Both:	3/148	0/48	3/28	0/20	0/20	0/32
Betweenness Centrality	Left:	24/74	8/24	6/14	1/10	2/10	7/16
	Right:	34/74	11/24	10/14	1/10	3/10	9/16
	Both:	58/148	19/48	16/28	2/20	5/20	16/32
Clustering Coefficient	Left:	1/74	0/24	0/14	0/10	0/10	1/16
	Right:	6/74	2/24	1/14	0/10	0/10	3/16
	Both:	7/148	2/48	1/28	0/20	0/20	4/32
Local Efficiency	Left:	0/74	0/24	0/14	0/10	0/10	0/16
	Right:	0/74	0/24	0/14	0/10	0/10	0/16
	Both:	0/148	0/48	0/28	0/20	0/20	0/32
Participation Coefficient	Left:	3/74	0/24	2/14	0/10	0/10	1/16
	Right:	4/74	1/24	2/14	0/10	0/10	1/16
	Both:	7/148	1/48	4/28	0/20	0/20	2/32

bioRxiv preprint doi: https://doi.org/10.1101/2023.12.23.573208; this version posted December 23, 2023. The copyright holder for this preprint (which was not certified by peer review) is the author/funder, who has granted bioRxiv a license to display the preprint in perpetuity. It is made available under aCC-BY-NC-ND 4.0 International license.

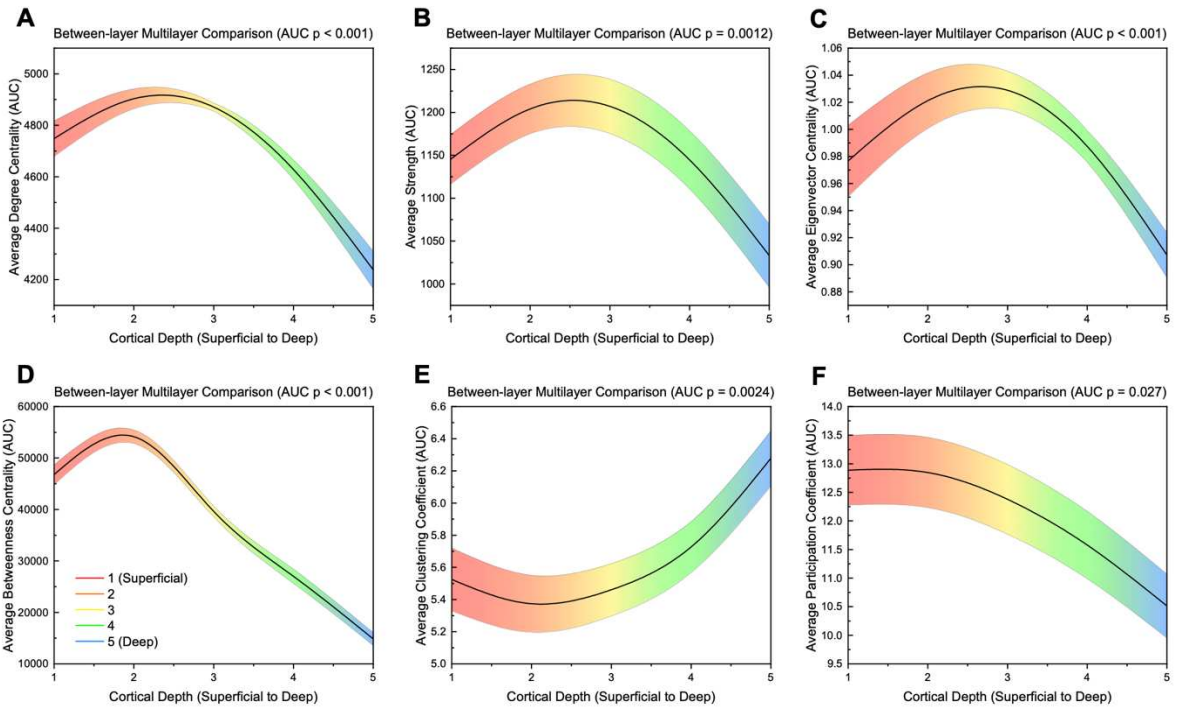

Figure 6. Area-under-the-curve (AUC) values across different layers for significant global measures ($p \leq 0.05$) for between-layer analysis. Significance was calculated using a one-way ANOVA. Spline interpolation was used for visualization. The mean value across participants at each layer is plotted while the shaded region indicates the standard error.

Between-layer Global

Significant between-layer global measures can be found in **Figure 6**. AUC values for all global measures can be found in **Table S8**. Average degree centrality ($p < 0.001$), average strength ($p = 0.0011$), average eigenvector centrality ($p < 0.001$), average betweenness centrality ($p < 0.001$), and average participation coefficient ($p = 0.027$) decreased from superficial (layer 1) to deep (layer 5) with all except average participation coefficient showing a peak in layers 2 and 3 (**Figure 6A–D, F**). Average clustering coefficient ($p = 0.0024$) increased from layer 1 to layer 5 with a slight decrease from layer 1 to layer 2 (**Figure 6E**). Average local efficiency was the only measure that showed no significant difference between layers (**Figure S19–20, Table S8**).

Between-layer Local

Brain regions with nodes that were significantly different using between-layer matrices can be found in **Table 6** (FDR correction with alpha = 0.01) (See **Table S9** for specific values and regions). Betweenness centrality had the largest number of significant nodes (57/148) followed by clustering coefficient (22/148) (**Table 6**). For betweenness centrality, most significant nodes were had the highest values in the superficial layers (layers 1 and 2) while for clustering coefficient, all significant nodes were highest in layer 5 (**Figure**

bioRxiv preprint doi: https://doi.org/10.1101/2023.12.23.573208; this version posted December 23, 2023. The copyright holder for this preprint (which was not certified by peer review) is the author/funder, who has granted bioRxiv a license to display the preprint in perpetuity. It is made available under aCC-BY-NC-ND 4.0 International license.

S21). In degree centrality, strength, eigenvector centrality, and betweenness centrality, the limbic region had the percentage of significant nodes within each region (**Table 6**). In betweenness centrality, frontal region nodes had the highest absolute number of significant nodes (20/48). In clustering coefficient (10/32) and participation coefficient (4/32), the temporal region had the most significant nodes (**Table 6**). Local efficiency had no significant nodes (**Table 6, Table S9, Figure S21**). The right hemisphere had more significant nodes than the left hemisphere for all measures (**Table 6**). Significant nodes were dispersed across different thickness levels, with betweenness centrality nodes leaning slightly more toward thicker regions (**Figure S22–S23**).

Table 6. Number of significant nodes within each brain region for between analysis. Significance was calculated from the area-under-the curve (AUC) values using a one-way ANOVA with an FDR correction (alpha = 0.01) to account for multiple comparisons [83, 84]. Details of nodal mapping to each region can be found in Table S1. Orange: hemisphere with the highest number of nodes; Yellow: measure with the highest number of nodes; Green: region within each measure with the highest number of nodes.

Network Measure	Hemisphere	All Regions	Frontal	Limbic	Occipital	Parietal	Temporal
Degree Centrality	Left:	1/74	0/24	1/14	0/10	0/10	0/16
	Right:	4/74	0/24	2/14	0/10	0/10	2/16
	Both:	5/148	0/48	3/28	0/20	0/20	2/32
Strength	Left:	1/74	0/24	1/14	0/10	0/10	0/16
	Right:	4/74	0/24	2/14	0/10	0/10	2/16
	Both:	5/148	0/48	3/28	0/20	0/20	2/32
Eigenvector Centrality	Left:	1/74	0/24	1/14	0/10	0/10	0/16
	Right:	2/74	0/24	2/14	0/10	0/10	0/16
	Both:	3/148	0/48	3/28	0/20	0/20	0/32
Betweenness Centrality	Left:	25/74	10/24	7/14	1/10	1/10	6/16
	Right:	32/74	10/24	11/14	1/10	2/10	8/16
	Both:	57/148	20/48	18/28	2/20	3/20	14/32
Clustering Coefficient	Left:	6/74	0/24	3/14	0/10	0/10	3/16
	Right:	16/74	3/24	5/14	1/10	0/10	7/16
	Both:	22/148	3/48	8/28	1/20	0/20	10/32
Local Efficiency	Left:	0/74	0/24	0/14	0/10	0/10	0/16
	Right:	0/74	0/24	0/14	0/10	0/10	0/16
	Both:	0/148	0/48	0/28	0/20	0/20	0/32
Participation Coefficient	Left:	2/74	0/24	1/14	0/10	0/10	1/16
	Right:	5/74	1/24	1/14	0/10	0/10	3/16
	Both:	7/148	1/48	2/28	0/20	0/20	4/32

bioRxiv preprint doi: https://doi.org/10.1101/2023.12.23.573208; this version posted December 23, 2023. The copyright holder for this preprint (which was not certified by peer review) is the author/funder, who has granted bioRxiv a license to display the preprint in perpetuity. It is made available under aCC-BY-NC-ND 4.0 International license.

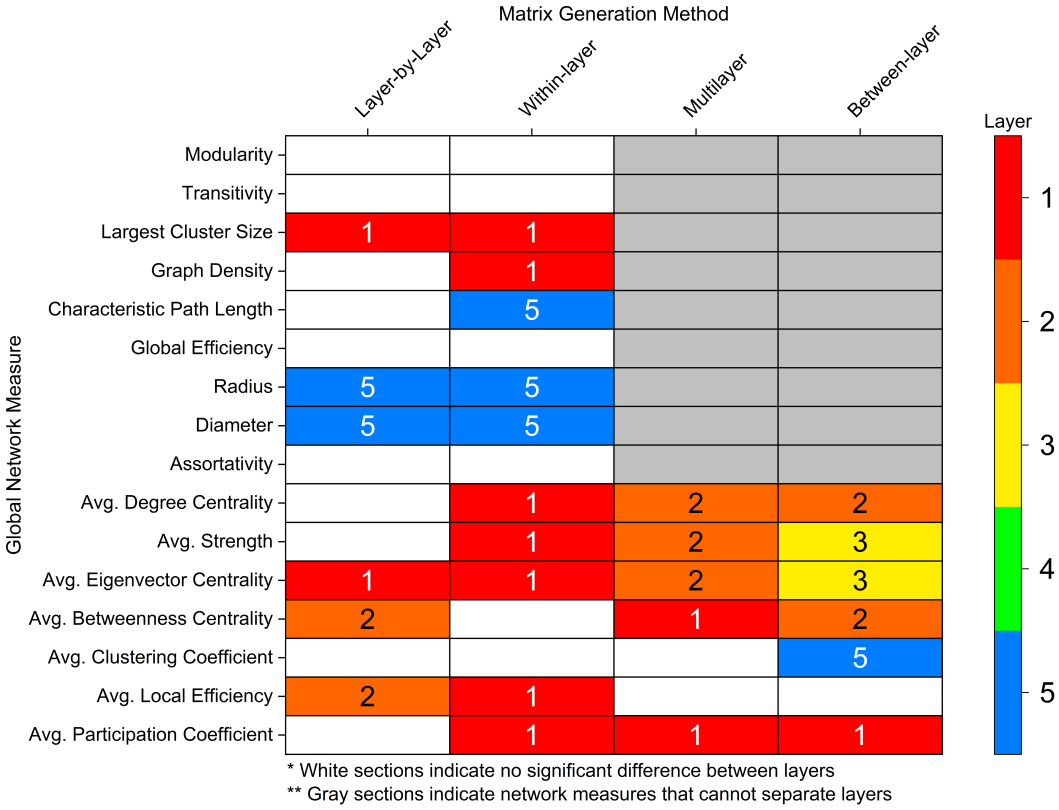

Figure 7. Layer with the highest area-under-the-curve (AUC) value across different global network measures methods ($p \leq 0.05$). Significance was calculated using a one-way ANOVA. White sections indicate no significant difference between layers. Gray sections indicate network measures that cannot separate effects of different layers.

Method Comparison

All four network measure methods (layer-by-layer, within-layer, multilayer, between-layer) identified global differences between layers (**Figure 7**). Layer-by-layer and within-layer methods showed an increase in integration-based global measures (radius and diameter) from layer 1 to layer 5; however, the within-layer approach identified an increase in characteristic path length as well. Similarly, layer-by-layer and within-layer approaches identified a decrease in largest cluster size from layer 1 to layer 5, with an additional decrease found in graph density using the within-layer method.

For nodal-averaged global measures, which can be applied to all four methods, measures generally decreased from superficial layers (1 and 2) to deeper layers (**Figure 7**). The layer-by-layer methodology identified significant differences in three measures (average eigenvector centrality, average betweenness centrality, and average local efficiency) while the within-layer approach found significant differences in five measures (average

bioRxiv preprint doi: https://doi.org/10.1101/2023.12.23.573208; this version posted December 23, 2023. The copyright holder for this preprint (which was not certified by peer review) is the author/funder, who has granted bioRxiv a license to display the preprint in perpetuity. It is made available under aCC-BY-NC-ND 4.0 International license.

degree centrality, average strength, average eigenvector centrality, average local efficiency, and average participation coefficient). The multilayer approach also found differences in five measures (average degree centrality, average strength, average eigenvector centrality, average betweenness centrality, and average participation coefficient). Interestingly, the between-layer method identified the most measures with significant differences between layers using six measures, with two measures (average strength and average eigenvector centrality) peaking in the middle layer. Additionally, the between-layer approach was the only method to identify a difference in average clustering coefficient which was the highest in layer 5.

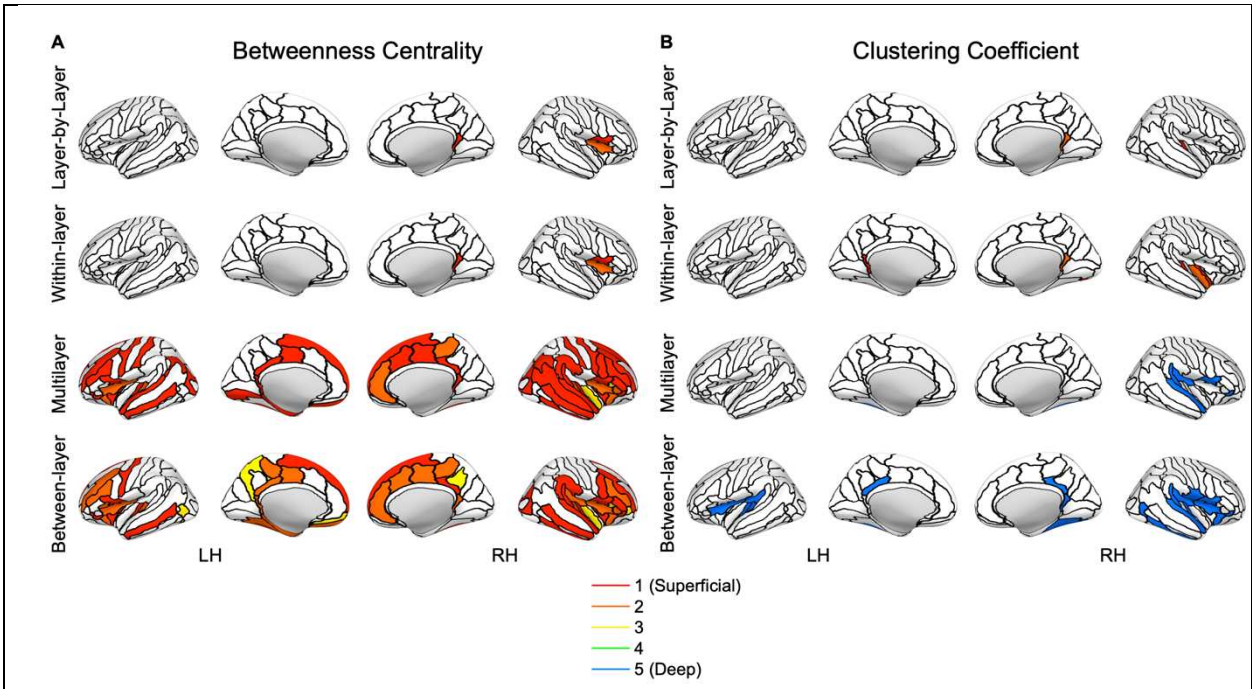

Figure 8. Nodes with significant differences between layers for each nodal measure pipeline (layer-by-layer, within-layer, multilayer, between-layer) for **(A)** betweenness centrality and **(B)** clustering coefficient. Significance was calculated from the area-under-the curve (AUC) values using a one-way ANOVA with an FDR correction (alpha = 0.01) to account for multiple comparisons [83, 84]. The colored section represents the layer with the highest value for the node. The nodes are based on the Destrieux atlas in FreeSurfer [67, 68]. LH: left hemisphere; RH: right hemisphere.

Similar to global measures, the multilayer-based approaches (within-layer, multilayer, between-layer) identified more nodal differences between layers than the layer-by-layer approach (**Table 3–6**). For example, the layer-by-layer method identified a maximum of four nodes with significant differences per measures compared to fifteen for within-layer (degree centrality), fifty-eight for multilayer (betweenness centrality), and fifty-seven for between-layer (betweenness centrality). Despite this, in a majority of measures for all four methods, the limbic region had the greatest number of nodes with significant differences between layers. The right hemisphere also had more significant nodes across all methods and measures (**Table 3–6**). The right (2.4127 ± 0.0306 mm; AVG ± SE) and left (2.4069 ± 0.0303 mm) hemispheres had comparable cortical thicknesses overall and across brain

bioRxiv preprint doi: https://doi.org/10.1101/2023.12.23.573208; this version posted December 23, 2023. The copyright holder for this preprint (which was not certified by peer review) is the author/funder, who has granted bioRxiv a license to display the preprint in perpetuity. It is made available under aCC-BY-NC-ND 4.0 International license.

regions (**Figure S24**). Additionally, while the thickness of significant nodes versus non-significant nodes was significantly larger in betweenness centrality metrics (multilayer, between-layer), the absolute difference between significant and non-significant nodes was typically less than 1 mm (**Figure S25**).

Two measures that showed a considerable benefit from the multilayer-based approach were betweenness centrality and clustering coefficient (**Figure 8**). For example, the multilayer and between-layer methods showed substantial increase in the number of nodes that had significant differences between layers. Similarly, the number of nodes with significant differences between layers in clustering coefficient increased using multilayer and between-layer methods. More importantly, however, is clustering coefficient in multilayer and between-layer approaches is the only measure to highlight the deepest layer as having the largest value. Likewise, the multilayer and between-layer methods are the only methods to include nodes that are the highest value in the middle layer (**Figure S16, S21**).

Discussion

Graph theory analysis of high-resolution (7T) resting-state fMRI revealed global and nodal network differences between cortical depths. Global integration measures (radius, diameter, characteristic path length) were higher in deeper layers while composition (largest cluster size, graph density, degree centrality, strength) and centrality (eigenvector centrality, betweenness centrality) measures were often higher in superficial layers (**Figure 7**).

Current literature exploring graph theory measures and overall laminar connectivity through networks in the human brain is very limited. Structural analysis of the human connectome using diffusion MRI combined with T_1-weighted anatomical imaging found qualitative differences in degree, strength, and betweenness centrality nodal distributions across cortical depths [88]; however, network-wide global calculations were absent. In a functional approach, Deshpande et al. found no global differences between layers using mean blind deconvoluted Pearson correlations from resting-state fMRI [89]. However, no threshold was used, enabling spurious correlations to impact the mean. Additionally, using the mean across the whole brain obfuscates any impact of a particular ROI. Our results, thus, significantly extend global and nodal network analysis of cortical architecture across the entire brain.

Our findings provide evidence of an advantage of applying of multilayer graph theory to connectomic analysis. While differences between layers were seen across all methodologies, the multilayer approach provided a greater identification of these differences through identifying more measures with larger significant differences (**Figure 7**). Previous connectomic studies have shown a benefit of applying a multilayer network framework [28-30]. For example, multilayer connectomics enables the integration of complex neuroimaging data (cortical lamina, frequency bands, multi-modal neuroimaging) [28-33, 57] and the creation of new network features. New network features can be used to explain neuroscientific findings, as in this work, or even enhance

bioRxiv preprint doi: https://doi.org/10.1101/2023.12.23.573208; this version posted December 23, 2023. The copyright holder for this preprint (which was not certified by peer review) is the author/funder, who has granted bioRxiv a license to display the preprint in perpetuity. It is made available under aCC-BY-NC-ND 4.0 International license.

machine learning workflows to better discriminate between disease states [90]. Future connectomics studies with available data should therefore consider using a multilayer framework to augment brain network modeling and analysis.

One particular benefit of multilayer analysis in laminar connectomics is the ability to discriminate between and incorporate the impact of within- and between-layer connections. While this comparison was limited to nodal averaged global measures and nodal values, there was still a stark comparison between within- and between-layer connections. When exploring layers individually (within-layer connections), the most superficial layer had the highest activation and is densely connected to itself while the deepest layer was relatively sparsely connected and took longer network paths to transmit information to different brain regions (**Figure 4,7**). However, in between layer connections, layer 1 becomes less important and the superficial-middle layers (layers 2 and 3) become integral for cortical connectivity (**Figure 6–7**). The superficial-middle layers (layers 2 and 3) had the highest between-layer degree, strength, and eigenvector centrality, indicating both layers are densely connected to other layers. Additionally, layer 2's significantly larger betweenness centrality demonstrates it is the most important layer for information flow between layers (**Figure 6–7)**. Lastly, the deepest layer had the highest clustering coefficient meaning it had the highest likelihood of forming local hubs (triangles) with other layers. Thus, within- and between-layer analysis provides evidence of a highly active superficial layer that utilizes layers 2 and 3 to transmit information to other cortical layers.

One important note to contextualize the above findings is that while activity and hubs of information flow can be identified, the direction of information flow cannot be delineated. Cortical layer architecture can have diverse connectivity patterns across layers and hierarchal schemes [34]. Therefore, it is important to recognize the correlation nature of this work rather than infer causality. Furthermore, while our results primarily focus on layers with the highest measure/activity, this does not imply that other layers are inactive.

The significance of connectivity patterns and characteristics for cortical depths differed across different brain regions. We identified extensive differences between layers in the frontal, limbic, and temporal brain regions (**Figure 8, Table 3–6**). Interestingly, the limbic cortex, often with the most significant regions per measures, typically has less layers than other brain regions [85]. Thus, cellular architecture may play a role in the ability for laminar fMRI, and potentially multilayer connectomics, to detect differences between cortical layers. Cortical thickness may also play a role in detecting differences between layers [91]. The regions (frontal, limbic, and temporal) with the most differences were often the thickest regions (**Figure S24**), with our results overlapping with previous studies [91]. Additionally, other factors that may impact cortical function and detectability including the neurite density index, orientation dispersion index, and myelin [91]. However, Fukutomi's et al. findings show a varied distribution across regions for these measures [91]. Despite this variation, hot-spots in these metrics near the posterior-ventral part of the cingulate gyrus and transverse temporal sulcus often overlap with significant nodes in our work. Therefore, our results indicate the need to contextualize layer fMRI results within cortical

bioRxiv preprint doi: https://doi.org/10.1101/2023.12.23.573208; this version posted December 23, 2023. The copyright holder for this preprint (which was not certified by peer review) is the author/funder, who has granted bioRxiv a license to display the preprint in perpetuity. It is made available under aCC-BY-NC-ND 4.0 International license.

metrics while providing a framework for potential regions (frontal, limbic, temporal) that may be suited for whole-brain laminar analysis.

On a global network level, there were high levels of activation in superficial layers when compared to deeper layers, in line with previous resting-state fMRI analyses reporting increased activation patterns in superficial cortical depths [43, 60, 62, 92]. Higher composition and centrality measures indicate a more robustly connected network (**Figure 7**). Additionally, at least within the same network (layer-by-layer and within-layer), deeper layers had significantly longer paths to transmit information, shown by higher global integration measures. It is, however, important to consider the pial vein bias [60], which increases gradient-echo BOLD signals from the deep to the more superficial parts of cortex. Further studies with alternative contrast mechanisms, which are less affected by the draining vein effect, are thus needed to determine whether the superficial cortical depths play a more critical role in the brain at rest, compared to the deeper aspects of the cortex.

Limitations

This study does have some limitations, both in terms of laminar analysis and connectomic analysis. Regarding our laminar analysis approach, the limitations of this study include biases associated with our fMRI pulse sequence, signal-to-noise ratio bias, the number of cortical depths chosen, the depth to cortical layer incongruence, and the impact of resting-state versus task-based paradigms. This work uses gradient-echo BOLD pulse sequences which may not be fully optimal for laminar analysis [43, 93]. Gradient-echo BOLD can be influenced largely by large draining vessels [60, 94-96], while spin-echo BOLD [97-100] and VAscular Space Occupancy (VASO) [48, 101] have been proposed as alternative fMRI contrasts for laminar analysis to address this large vein bias [43, 93]. However, VASO and spin-echo BOLD have lower sensitivity and several practical challenges [102]. Similarly, signal-to-noise ratio (SNR) can vary at different cortical depths. For example, depths within the middle of the cortex will contain less tissue boundary effects compared to the depths near the pial and white matter surfaces [103]. This difference may be further exacerbated since the thickness and functionality of cortical layers can change based on brain region [85-87] and cortical curvature [104-107]. However, as shown above for nodal analysis, thickness varied across statistically significant nodes suggesting our results are not purely a function of cortical thickness (**Figure S6–S7, S12–S13, S17–S18, S22–S23, S24–S25**). Cortical curvature was not explored, and future laminar work should include the anatomical constraints of the cortex to address this. In addition to the location of the cortical depths chosen, the number of depths can affect the results. Other studies have used a smaller number of depths to ensure independence between depths [108], six depths to match the number of cortical layers [109], or even a larger amount that showed an improved detection of cortical responses [110]. The number of depths chosen should balance independence, cortical response detection, and computational demands from a higher depth count. Furthermore, as mentioned above, the cortical depths do not directly equate to cytoarchitectural cortical layers. Lastly, this study used resting-state fMRI to study whole-brain connectivity; however, laminar resting-state fMRI activation patterns may be different than laminar

bioRxiv preprint doi: https://doi.org/10.1101/2023.12.23.573208; this version posted December 23, 2023. The copyright holder for this preprint (which was not certified by peer review) is the author/funder, who has granted bioRxiv a license to display the preprint in perpetuity. It is made available under aCC-BY-NC-ND 4.0 International license.

task-based patterns [109], limiting the broad applicability to task-based laminar paradigms. Despite potential activation pattern differences, the underlying anatomical basis of resting-state connections [63-66] can still inform task-based paradigms.

Regarding our connectomic approach, limitations include the parcellation choice, thresholding methodology, and multilayer measure calculations. Parcellation choice can impact graph theory results [111, 112]. This work used the Destrieux atlas in FreeSurfer [67, 68], which is based on anatomical nomenclature. However, an atlas derived from functional connectivity may be more appropriate for a functional analysis study [113]. Additionally, for laminar analysis, a custom atlas using laminar cytoarchitecture and cortical thickness may improve the accuracy of the results. As mentioned above, graph theory measures are directly impacted by thresholding the network [114]. AUC analysis attempts to correct for this thresholding bias but still may be inadequate for eliminating thresholding's effect on network characteristics.

Increased BOLD signal in superficial vs. deeper layers may be due to vascular-related bias [60, 94-96, 109]. One might conclude that the present results reflect vascular biases. However, the most superficial depth was excluded in this work to reduce this bias. Additionally, some composition and centrality measures peaked in layers 2 and 3, notably average strength, suggesting that some observed effects are not explainable by biases in superficial layers (**Figure 7**, **S6–S7, S12–S13, S17–S18, S22–S23, S24–S25**).

Conclusion

Our multilayer connectomics findings demonstrate global and nodal network differences between cortical depths that can be more aptly identified through the multilayer approach compared to traditional single layer connectomics. These results demonstrate the validity of the multilayer connectomic framework on laminar fMRI and provide a methodological foundation for future multilayer laminar studies. Future work should further explore the intersection of connectomics and laminar studies and address current methodological constraints.

Supporting Information

Author Contributions

Parker Kotlarz: Conceptualization; Methodology; Software; Validation; Formal analysis; Investigation; Data curation; Writing – original draft; Writing – review & editing; Visualization.
Kaisu Lankinen: Conceptualization; Methodology; Software; Investigation; Writing – review & editing; Visualization; Supervision.
Maria Hakonen: Methodology; Software; Investigation; Data curation; Writing – review & editing.
Tori Turpin: Investigation; Writing – review & editing.
Jonathan R. Polimeni: Methodology; Software; Writing – review & editing.

bioRxiv preprint doi: https://doi.org/10.1101/2023.12.23.573208; this version posted December 23, 2023. The copyright holder for this preprint (which was not certified by peer review) is the author/funder, who has granted bioRxiv a license to display the preprint in perpetuity. It is made available under aCC-BY-NC-ND 4.0 International license.

Jyrki Ahveninen: Conceptualization; Methodology; Investigation; Writing – review & editing; Supervision; Project administration; Funding acquisition.

Funding Information
Supported by R01DC017991, R01DC016765, R01DC016915 and P41-EB030006.

References

1. Farahani, F.V., W. Karwowski, and N.R. Lighthall, *Application of Graph Theory for Identifying Connectivity Patterns in Human Brain Networks: A Systematic Review.* Front Neurosci, 2019. **13**: p. 585.
2. Milano, M., P.H. Guzzi, and M. Cannataro, *Network building and analysis in connectomics studies: a review of algorithms, databases and technologies.* Network Modeling Analysis in Health Informatics and Bioinformatics, 2019. **8**(1).
3. Rubinov, M. and O. Sporns, *Complex network measures of brain connectivity: uses and interpretations.* Neuroimage, 2010. **52**(3): p. 1059-69.
4. Griffa, A., et al., *Structural connectomics in brain diseases.* Neuroimage, 2013. **80**: p. 515-26.
5. Yeh, C.H., et al., *Mapping Structural Connectivity Using Diffusion MRI: Challenges and Opportunities.* J Magn Reson Imaging, 2021. **53**(6): p. 1666-1682.
6. Meoded, A., N.A. Goldenberg, and T. Huisman, *Structural Connectomics: State of the Art and Applications in Pediatric Neurodevelopmental Disorders, Neuro-Oncology, and Arterial Ischemic Stroke.* J Pediatr, 2020. **221S**: p. S37-S42.
7. De Vico Fallani, F., et al., *Graph analysis of functional brain networks: practical issues in translational neuroscience.* Philos Trans R Soc Lond B Biol Sci, 2014. **369**(1653).
8. Xia, M. and Y. He, *Functional connectomics from a "big data" perspective.* Neuroimage, 2017. **160**: p. 152-167.
9. Smith, S.M., et al., *Functional connectomics from resting-state fMRI.* Trends Cogn Sci, 2013. **17**(12): p. 666-82.
10. Matthews, P.M. and A. Hampshire, *Clinical Concepts Emerging from fMRI Functional Connectomics.* Neuron, 2016. **91**(3): p. 511-28.
11. Sadaghiani, S., M.J. Brookes, and S. Baillet, *Connectomics of human electrophysiology.* Neuroimage, 2022. **247**: p. 118788.
12. Jacob, Y., et al., *Neural correlates of rumination in major depressive disorder: A brain network analysis.* Neuroimage Clin, 2020. **25**: p. 102142.
13. Benito-Leon, J., et al., *Graph theory analysis of resting-state functional magnetic resonance imaging in essential tremor.* Hum Brain Mapp, 2019. **40**(16): p. 4686-4702.
14. Kotlarz, P., J.C. Nino, and M. Febo, *Connectomic analysis of Alzheimer's disease using percolation theory.* Netw Neurosci, 2022. **6**(1): p. 213-233.
15. Fleischer, V., et al., *Graph Theoretical Framework of Brain Networks in Multiple Sclerosis: A Review of Concepts.* Neuroscience, 2019. **403**: p. 35-53.

bioRxiv preprint doi: https://doi.org/10.1101/2023.12.23.573208; this version posted December 23, 2023. The copyright holder for this preprint (which was not certified by peer review) is the author/funder, who has granted bioRxiv a license to display the preprint in perpetuity. It is made available under aCC-BY-NC-ND 4.0 International license.

16. Dadario, N.B., et al., *Reducing the Cognitive Footprint of Brain Tumor Surgery.* Front Neurol, 2021. **12**: p. 711646.
17. Gleichgerrcht, E., et al., *Temporal Lobe Epilepsy Surgical Outcomes Can Be Inferred Based on Structural Connectome Hubs: A Machine Learning Study.* Ann Neurol, 2020. **88**(5): p. 970-983.
18. Hart, M.G., S.J. Price, and J. Suckling, *Connectome analysis for pre-operative brain mapping in neurosurgery.* Br J Neurosurg, 2016. **30**(5): p. 506-17.
19. Ahsan, S.A., et al., *Beyond eloquence and onto centrality: a new paradigm in planning supratentorial neurosurgery.* J Neurooncol, 2020. **146**(2): p. 229-238.
20. Tavakol, S., et al., *Neuroimaging and connectomics of drug-resistant epilepsy at multiple scales: From focal lesions to macroscale networks.* Epilepsia, 2019. **60**(4): p. 593-604.
21. Caeyenberghs, K., et al., *Mapping the functional connectome in traumatic brain injury: What can graph metrics tell us?* Neuroimage, 2017. **160**: p. 113-123.
22. Chen, V.C., et al., *Connectome analysis of brain functional network alterations in breast cancer survivors with and without chemotherapy.* PLoS One, 2020. **15**(5): p. e0232548.
23. Lei, D., et al., *Changes in the brain structural connectome after a prospective randomized clinical trial of lithium and quetiapine treatment in youth with bipolar disorder.* Neuropsychopharmacology, 2021. **46**(7): p. 1315-1323.
24. Filippi, M., et al., *The human functional connectome in neurodegenerative diseases: relationship to pathology and clinical progression.* Expert Rev Neurother, 2023. **23**(1): p. 59-73.
25. Yun, J.Y. and Y.K. Kim, *Graph theory approach for the structural-functional brain connectome of depression.* Prog Neuropsychopharmacol Biol Psychiatry, 2021. **111**: p. 110401.
26. Boccaletti, S., et al., *The structure and dynamics of multilayer networks.* Phys Rep, 2014. **544**(1): p. 1-122.
27. Kivela, M., et al., *Multilayer networks.* Journal of Complex Networks, 2014. **2**(3): p. 203-271.
28. Betzel, R.F. and D.S. Bassett, *Multi-scale brain networks.* Neuroimage, 2017. **160**: p. 73-83.
29. De Domenico, M., *Multilayer modeling and analysis of human brain networks.* Gigascience, 2017. **6**(5): p. 1-8.
30. Vaiana, M. and S.F. Muldoon, *Multilayer Brain Networks.* Journal of Nonlinear Science, 2018. **30**(5): p. 2147-2169.
31. Buldu, J.M. and M.A. Porter, *Frequency-based brain networks: From a multiplex framework to a full multilayer description.* Netw Neurosci, 2018. **2**(4): p. 418-441.
32. Breedt, L.C., et al., *Multimodal multilayer network centrality relates to executive functioning.* Network Neuroscience, 2023. **7**(1): p. 299-321.
33. Casas-Roma, J., et al., *Applying multilayer analysis to morphological, structural, and functional brain networks to identify relevant dysfunction patterns.* Netw Neurosci, 2022. **6**(3): p. 916-933.
34. Felleman, D.J. and D.C. Van Essen, *Distributed hierarchical processing in the primate cerebral cortex.* Cereb Cortex, 1991. **1**(1): p. 1-47.

bioRxiv preprint doi: https://doi.org/10.1101/2023.12.23.573208; this version posted December 23, 2023. The copyright holder for this preprint (which was not certified by peer review) is the author/funder, who has granted bioRxiv a license to display the preprint in perpetuity. It is made available under aCC-BY-NC-ND 4.0 International license.

35. Rockland, K.S. and D.N. Pandya, *Laminar origins and terminations of cortical connections of the occipital lobe in the rhesus monkey.* Brain Res, 1979. **179**(1): p. 3-20.
36. Zeki, S., *The Rough Seas of Cortical Cartography.* Trends Neurosci, 2018. **41**(5): p. 242-244.
37. Schroeder, C.E., et al., *Somatosensory input to auditory association cortex in the macaque monkey.* J Neurophysiol, 2001. **85**(3): p. 1322-7.
38. Schroeder, C.E. and J.J. Foxe, *The timing and laminar profile of converging inputs to multisensory areas of the macaque neocortex.* Brain Res Cogn Brain Res, 2002. **14**(1): p. 187-98.
39. Rockland, K.S., *What do we know about laminar connectivity?* Neuroimage, 2019. **197**: p. 772-784.
40. Finn, E.S., et al., *Layer-dependent activity in human prefrontal cortex during working memory.* Nat Neurosci, 2019. **22**(10): p. 1687-1695.
41. Norris, D.G. and J.R. Polimeni, *Laminar (f)MRI: A short history and future prospects.* Neuroimage, 2019. **197**: p. 643-649.
42. Polimeni, J.R., et al., *Analysis strategies for high-resolution UHF-fMRI data.* Neuroimage, 2018. **168**: p. 296-320.
43. Huber, L., et al., *Layer-dependent functional connectivity methods.* Prog Neurobiol, 2021. **207**: p. 101835.
44. Markuerkiaga, I., M. Barth, and D.G. Norris, *A cortical vascular model for examining the specificity of the laminar BOLD signal.* Neuroimage, 2016. **132**: p. 491-8.
45. Lankinen, K., et al., *Cortical depth profiles of auditory and visual 7 T functional MRI responses in human superior temporal areas.* Hum Brain Mapp, 2023. **44**(2): p. 362-372.
46. Fracasso, A., et al., *Laminar imaging of positive and negative BOLD in human visual cortex at 7T.* Neuroimage, 2018. **164**: p. 100-111.
47. Gau, R., et al., *Resolving multisensory and attentional influences across cortical depth in sensory cortices.* Elife, 2020. **9**.
48. Chai, Y., et al., *Topographical and laminar distribution of audiovisual processing within human planum temporale.* Prog Neurobiol, 2021. **205**: p. 102121.
49. Klein, B.P., et al., *Cortical depth dependent population receptive field attraction by spatial attention in human V1.* Neuroimage, 2018. **176**: p. 301-312.
50. Kok, P., et al., *Selective Activation of the Deep Layers of the Human Primary Visual Cortex by Top-Down Feedback.* Curr Biol, 2016. **26**(3): p. 371-6.
51. Lawrence, S.J., D.G. Norris, and F.P. de Lange, *Dissociable laminar profiles of concurrent bottom-up and top-down modulation in the human visual cortex.* Elife, 2019. **8**.
52. Muckli, L., et al., *Contextual Feedback to Superficial Layers of V1.* Curr Biol, 2015. **25**(20): p. 2690-5.
53. De Martino, F., et al., *Frequency preference and attention effects across cortical depths in the human primary auditory cortex.* Proc Natl Acad Sci U S A, 2015. **112**(52): p. 16036-41.
54. Moerel, M., et al., *Evaluating the Columnar Stability of Acoustic Processing in the Human Auditory Cortex.* J Neurosci, 2018. **38**(36): p. 7822-7832.

bioRxiv preprint doi: https://doi.org/10.1101/2023.12.23.573208; this version posted December 23, 2023. The copyright holder for this preprint (which was not certified by peer review) is the author/funder, who has granted bioRxiv a license to display the preprint in perpetuity. It is made available under aCC-BY-NC-ND 4.0 International license.

55. Moerel, M., et al., *Processing complexity increases in superficial layers of human primary auditory cortex.* Sci Rep, 2019. **9**(1): p. 5502.
56. Wu, P.Y., et al., *Feature-dependent intrinsic functional connectivity across cortical depths in the human auditory cortex.* Sci Rep, 2018. **8**(1): p. 13287.
57. Shamir, I. and Y. Assaf, *Expanding connectomics to the laminar level: A perspective.* Network Neuroscience, 2023: p. 1-12.
58. Shamir, I. and Y. Assaf, *An MRI-Based, Data-Driven Model of Cortical Laminar Connectivity.* Neuroinformatics, 2021. **19**(2): p. 205-218.
59. Wei, Y., et al., *Multiscale examination of cytoarchitectonic similarity and human brain connectivity.* Netw Neurosci, 2019. **3**(1): p. 124-137.
60. Polimeni, J.R., et al., *Laminar analysis of 7T BOLD using an imposed spatial activation pattern in human V1.* Neuroimage, 2010. **52**(4): p. 1334-46.
61. Finn, E.S., L. Huber, and P.A. Bandettini, *Higher and deeper: Bringing layer fMRI to association cortex.* Prog Neurobiol, 2021. **207**: p. 101930.
62. Huber, L.R., et al., *LayNii: A software suite for layer-fMRI.* Neuroimage, 2021. **237**: p. 118091.
63. Adachi, Y., et al., *Functional connectivity between anatomically unconnected areas is shaped by collective network-level effects in the macaque cortex.* Cereb Cortex, 2012. **22**(7): p. 1586-92.
64. van den Heuvel, M.P., et al., *Multimodal analysis of cortical chemoarchitecture and macroscale fMRI resting-state functional connectivity.* Hum Brain Mapp, 2016. **37**(9): p. 3103-13.
65. Honey, C.J., et al., *Predicting human resting-state functional connectivity from structural connectivity.* Proc Natl Acad Sci U S A, 2009. **106**(6): p. 2035-40.
66. Turk, E., L.H. Scholtens, and M.P. van den Heuvel, *Cortical chemoarchitecture shapes macroscale effective functional connectivity patterns in macaque cerebral cortex.* Hum Brain Mapp, 2016. **37**(5): p. 1856-65.
67. Destrieux, C., et al., *Automatic parcellation of human cortical gyri and sulci using standard anatomical nomenclature.* Neuroimage, 2010. **53**(1): p. 1-15.
68. Fischl, B., et al., *Automatically parcellating the human cerebral cortex.* Cereb Cortex, 2004. **14**(1): p. 11-22.
69. Mareyam, A., et al. *A 64-Channel 7T array coil for accelerated brain MRI*. in *Proceedings of the International Society for Magnetic Resonance in Medicine*. 2020.
70. van der Kouwe, A.J.W., et al., *Brain morphometry with multiecho MPRAGE.* Neuroimage, 2008. **40**(2): p. 559-569.
71. Zaretskaya, N., et al., *Advantages of cortical surface reconstruction using submillimeter 7 T MEMPRAGE.* Neuroimage, 2018. **165**: p. 11-26.
72. Setsompop, K., et al., *Blipped-controlled aliasing in parallel imaging for simultaneous multislice echo planar imaging with reduced g-factor penalty.* Magn Reson Med, 2012. **67**(5): p. 1210-24.
73. Fischl, B., *FreeSurfer.* NeuroImage, 2012. **62**(2): p. 774-781.
74. Smith, S.M., et al., *Advances in functional and structural MR image analysis and implementation as FSL.* Neuroimage, 2004. **23 Suppl 1**: p. S208-19.

bioRxiv preprint doi: https://doi.org/10.1101/2023.12.23.573208; this version posted December 23, 2023. The copyright holder for this preprint (which was not certified by peer review) is the author/funder, who has granted bioRxiv a license to display the preprint in perpetuity. It is made available under aCC-BY-NC-ND 4.0 International license.

75. Andersson, J.L., S. Skare, and J. Ashburner, *How to correct susceptibility distortions in spin-echo echo-planar images: application to diffusion tensor imaging.* Neuroimage, 2003. **20**(2): p. 870-88.
76. Glover, G.H., T.Q. Li, and D. Ress, *Image-based method for retrospective correction of physiological motion effects in fMRI: RETROICOR.* Magn Reson Med, 2000. **44**(1): p. 162-7.
77. Greve, D.N. and B. Fischl, *Accurate and robust brain image alignment using boundary-based registration.* Neuroimage, 2009. **48**(1): p. 63-72.
78. Finn, E.S., et al., *Functional connectome fingerprinting: identifying individuals using patterns of brain connectivity.* Nat Neurosci, 2015. **18**(11): p. 1664-71.
79. Menon, S.S. and K. Krishnamurthy, *A Comparison of Static and Dynamic Functional Connectivities for Identifying Subjects and Biological Sex Using Intrinsic Individual Brain Connectivity.* Sci Rep, 2019. **9**(1): p. 5729.
80. Cabral, J., et al., *Cognitive performance in healthy older adults relates to spontaneous switching between states of functional connectivity during rest.* Sci Rep, 2017. **7**(1): p. 5135.
81. Puetz, V.B., et al., *Altered brain network integrity after childhood maltreatment: A structural connectomic DTI-study.* Hum Brain Mapp, 2017. **38**(2): p. 855-868.
82. Schill, J., et al., *Parkinson's disease speech production network as determined by graph-theoretical network analysis.* Network Neuroscience, 2023: p. 1-19.
83. Groppe, D., *Bonferroni-Holm Correction for Multiple Comparisons*. 2023: MATLAB Central File Exchange.
84. Holm, S., *A Simple Sequentially Rejective Multiple Test Procedure.* Scandinavian Journal of Statistics, 1979. **6**(2): p. 65-70.
85. Barbas, H., *General cortical and special prefrontal connections: principles from structure to function.* Annu Rev Neurosci, 2015. **38**: p. 269-89.
86. Ding, S.L., et al., *Parcellation of human temporal polar cortex: a combined analysis of multiple cytoarchitectonic, chemoarchitectonic, and pathological markers.* J Comp Neurol, 2009. **514**(6): p. 595-623.
87. Zachlod, D., et al., *Four new cytoarchitectonic areas surrounding the primary and early auditory cortex in human brains.* Cortex, 2020. **128**: p. 1-21.
88. Shamir, I., et al., *Modelling the laminar connectome of the human brain.* Brain Struct Funct, 2022. **227**(6): p. 2153-2165.
89. Deshpande, G., Y. Wang, and J. Robinson, *Resting state fMRI connectivity is sensitive to laminar connectional architecture in the human brain.* Brain Inform, 2022. **9**(1): p. 2.
90. Zhu, Y., et al., *Abnormality of Functional Connections in the Resting State Brains of Schizophrenics.* Front Hum Neurosci, 2022. **16**: p. 799881.
91. Fukutomi, H., et al., *Neurite imaging reveals microstructural variations in human cerebral cortical gray matter.* Neuroimage, 2018. **182**: p. 488-499.
92. Guidi, M., et al., *Cortical laminar resting-state signal fluctuations scale with the hypercapnic blood oxygenation level-dependent response.* Hum Brain Mapp, 2020. **41**(8): p. 2014-2027.
93. Bandettini, P.A., L. Huber, and E.S. Finn, *Challenges and opportunities of mesoscopic brain mapping with fMRI.* Current Opinion in Behavioral Sciences, 2021. **40**: p. 189-200.

bioRxiv preprint doi: https://doi.org/10.1101/2023.12.23.573208; this version posted December 23, 2023. The copyright holder for this preprint (which was not certified by peer review) is the author/funder, who has granted bioRxiv a license to display the preprint in perpetuity. It is made available under aCC-BY-NC-ND 4.0 International license.

94. Markuerkiaga, I., M. Barth, and D.G. Norris, *A cortical vascular model for examining the specificity of the laminar BOLD signal.* Neuroimage, 2016. **132**: p. 491-498.
95. Olman, C.A., S. Inati, and D.J. Heeger, *The effect of large veins on spatial localization with GE BOLD at 3 T: Displacement, not blurring.* Neuroimage, 2007. **34**(3): p. 1126-35.
96. Turner, R., *How much cortex can a vein drain? Downstream dilution of activation-related cerebral blood oxygenation changes.* Neuroimage, 2002. **16**(4): p. 1062-7.
97. Duong, T.Q., et al., *Microvascular BOLD contribution at 4 and 7 T in the human brain: gradient-echo and spin-echo fMRI with suppression of blood effects.* Magn Reson Med, 2003. **49**(6): p. 1019-27.
98. Uludag, K., B. Muller-Bierl, and K. Ugurbil, *An integrative model for neuronal activity-induced signal changes for gradient and spin echo functional imaging.* Neuroimage, 2009. **48**(1): p. 150-65.
99. Yacoub, E., et al., *Spin-echo fMRI in humans using high spatial resolutions and high magnetic fields.* Magn Reson Med, 2003. **49**(4): p. 655-64.
100. Zhao, F., P. Wang, and S.G. Kim, *Cortical depth-dependent gradient-echo and spin-echo BOLD fMRI at 9.4T.* Magn Reson Med, 2004. **51**(3): p. 518-24.
101. Chai, Y., et al., *Integrated VASO and perfusion contrast: A new tool for laminar functional MRI.* Neuroimage, 2020. **207**: p. 116358.
102. Moerel, M., et al., *Using high spatial resolution fMRI to understand representation in the auditory network.* Prog Neurobiol, 2021. **207**: p. 101887.
103. Blazejewska, A.I., et al., *Intracortical smoothing of small-voxel fMRI data can provide increased detection power without spatial resolution losses compared to conventional large-voxel fMRI data.* Neuroimage, 2019. **189**: p. 601-614.
104. Fatterpekar, G.M., et al., *MR microscopy of normal human brain.* Magn Reson Imaging Clin N Am, 2003. **11**(4): p. 641-53.
105. Hilgetag, C.C. and H. Barbas, *Role of mechanical factors in the morphology of the primate cerebral cortex.* PLoS Comput Biol, 2006. **2**(3): p. e22.
106. Van Essen, D.C. and J.H. Maunsell, *Two-dimensional maps of the cerebral cortex.* J Comp Neurol, 1980. **191**(2): p. 255-81.
107. Fischl, B. and A.M. Dale, *Measuring the thickness of the human cerebral cortex from magnetic resonance images.* Proc Natl Acad Sci U S A, 2000. **97**(20): p. 11050-5.
108. Sharoh, D., et al., *Laminar specific fMRI reveals directed interactions in distributed networks during language processing.* Proc Natl Acad Sci U S A, 2019. **116**(42): p. 21185-21190.
109. Pais-Roldan, P., et al., *Cortical depth-dependent human fMRI of resting-state networks using EPIK.* Front Neurosci, 2023. **17**: p. 1151544.
110. Huber, L., et al., *High-Resolution CBV-fMRI Allows Mapping of Laminar Activity and Connectivity of Cortical Input and Output in Human M1.* Neuron, 2017. **96**(6): p. 1253-1263 e7.
111. Albers, K.J., et al., *Using connectomics for predictive assessment of brain parcellations.* Neuroimage, 2021. **238**: p. 118170.

bioRxiv preprint doi: https://doi.org/10.1101/2023.12.23.573208; this version posted December 23, 2023. The copyright holder for this preprint (which was not certified by peer review) is the author/funder, who has granted bioRxiv a license to display the preprint in perpetuity. It is made available under aCC-BY-NC-ND 4.0 International license.

112. Arslan, S., et al., *Human brain mapping: A systematic comparison of parcellation methods for the human cerebral cortex.* Neuroimage, 2018. **170**: p. 5-30.
113. Schaefer, A., et al., *Local-Global Parcellation of the Human Cerebral Cortex from Intrinsic Functional Connectivity MRI.* Cereb Cortex, 2018. **28**(9): p. 3095-3114.
114. Osmanlioglu, Y., et al., *Connectomic consistency: a systematic stability analysis of structural and functional connectivity.* J Neural Eng, 2020. **17**(4): p. 045004.